



UNIVERSIDAD DE INVESTIGACIÓN DE TECNOLOGÍA EXPERIMENTAL YACHAY

Escuela de Ciencias Matemáticas y Computacionales

TÍTULO: Interferometry Computation of Advanced Land Observing Satellite (ALOS-2) Data for the Northern Ecuador Region

Trabajo de integración curricular presentado como requisito para la obtención del título de Ingeniero en Tecnologías de la Información.

Autor:

Goyes Gordon Jhon Manuel

Tutor:

Pineda Arias Israel Gustavo, Ph.D.

Cotutor:

Foster Anna Elizabeth, Ph.D.

Urcuquí, Agosto 2022

Urququí, 11 de agosto de 2022

SECRETARÍA GENERAL
ESCUELA DE CIENCIAS MATEMÁTICAS Y COMPUTACIONALES
CARRERA DE TECNOLOGÍAS DE LA INFORMACIÓN
ACTA DE DEFENSA No. UITEY-ITE-2022-00022-AD

En la ciudad de San Miguel de Urququí, Provincia de Imbabura, a los 11 días del mes de agosto de 2022, a las 11:00 horas, en el Aula S_CAN de la Universidad de Investigación de Tecnología Experimental Yachay y ante el Tribunal Calificador, integrado por los docentes:

Presidente Tribunal de Defensa	Dr. ANTON CASTRO, FRANCESC, Ph.D.
Miembro No Tutor	Dr. ARMAS ARCINIEGA, JULIO JOAQUIN, Ph.D.
Tutor	Dr. PINEDA ARIAS, ISRAEL GUSTAVO, Ph.D.

Se presenta el(la) señor(ita) estudiante **GOYES GORDON, JHON MANUEL**, con cédula de identidad No. **0401836259**, de la **ESCUELA DE CIENCIAS MATEMÁTICAS Y COMPUTACIONALES**, de la Carrera de **TECNOLOGÍAS DE LA INFORMACIÓN**, aprobada por el Consejo de Educación Superior (CES), mediante Resolución **RPC-SO-43-No.496-2014**, con el objeto de rendir la sustentación de su trabajo de titulación denominado: **Interferometry Computation of Advanced Land Observing Satellite (ALOS-2) Data for the Northern Ecuador Region**, previa a la obtención del título de **INGENIERO/A EN TECNOLOGÍAS DE LA INFORMACIÓN**.

El citado trabajo de titulación, fue debidamente aprobado por el(los) docente(s):

Tutor Dr. PINEDA ARIAS, ISRAEL GUSTAVO, Ph.D.

Y recibió las observaciones de los otros miembros del Tribunal Calificador, las mismas que han sido incorporadas por el(la) estudiante.

Previamente cumplidos los requisitos legales y reglamentarios, el trabajo de titulación fue sustentado por el(la) estudiante y examinado por los miembros del Tribunal Calificador. Escuchada la sustentación del trabajo de titulación, que integró la exposición de el(la) estudiante sobre el contenido de la misma y las preguntas formuladas por los miembros del Tribunal, se califica la sustentación del trabajo de titulación con las siguientes calificaciones:

Tipo	Docente	Calificación
Miembro Tribunal De Defensa	Dr. ARMAS ARCINIEGA, JULIO JOAQUIN, Ph.D.	8,5
Presidente Tribunal De Defensa	Dr. ANTON CASTRO, FRANCESC, Ph.D.	8,0
Tutor	Dr. PINEDA ARIAS, ISRAEL GUSTAVO, Ph.D.	10,0

Lo que da un promedio de: **8.8 (Ocho punto Ocho)**, sobre 10 (diez), equivalente a: **APROBADO**

Para constancia de lo actuado, firman los miembros del Tribunal Calificador, el/la estudiante y el/la secretario ad-hoc.


GOYES GORDON, JHON MANUEL
Estudiante


Dr. ANTON CASTRO, FRANCESC, Ph.D.
Presidente Tribunal de Defensa


Dr. PINEDA ARIAS, ISRAEL GUSTAVO, Ph.D.
Tutor


Dr. ARMAS ARCINIEGA, JULIO JOAQUIN, Ph.D.
Miembro No Tutor



MEDINA BRITO, DAYSY MARGARITA
Secretario Ad-hoc

Autoría

Yo, **Jhon Manuel Goyes Gordon**, con cédula de identidad **0401836259**, declaro que las ideas, juicios, valoraciones, interpretaciones, consultas bibliográficas, definiciones y conceptualizaciones expuestas en el presente trabajo; así cómo, los procedimientos y herramientas utilizadas en la investigación, son de absoluta responsabilidad de el autor del trabajo de integración curricular. Así mismo, me acojo a los reglamentos internos de la Universidad de Investigación de Tecnología Experimental Yachay.

Urcuquí, Agosto del 2022.

Jhon Manuel Goyes Gordon

CI: 0401836259

Autorización de publicación

Yo, **Jhon Manuel Goyes Gordon**, con cédula de identidad **0401836259**, cedo a la Universidad de Tecnología Experimental Yachay, los derechos de publicación de la presente obra, sin que deba haber un reconocimiento económico por este concepto. Declaro además que el texto del presente trabajo de titulación no podrá ser cedido a ninguna empresa editorial para su publicación u otros fines, sin contar previamente con la autorización escrita de la Universidad.

Asimismo, autorizo a la Universidad que realice la digitalización y publicación de este trabajo de integración curricular en el repositorio virtual, de conformidad a lo dispuesto en el Art. 144 de la Ley Orgánica de Educación Superior.

Urcuquí, Agosto del 2022.

Jhon Manuel Goyes Gordon

CI: 0401836259

Dedication

*“To my parents Manuel and Felisa, to my sister Victoria and all my family and friends
for all their support during this journey.”*

Jhon Goyes

Acknowledgments

I cannot begin to express my thanks to my tutor Israel Pineda Ph. D., who never wavered in their support bringing me their valuable advice and practical suggestions. I would also like to extend my deepest gratitude to my cotutor Ana E. Foster Ph. D., who always supported and nurtured me with her invaluable contribution and constructive advice. The elaboration of my dissertation would not have been possible without the support of Eric O. Lindsey Ph. D., who was instrumental in introducing me to the InSAR processing and its extensive knowledge. I'm extremely grateful to Rafael Almeida Ph. D., someone whose help cannot be overestimated for his suggestions and helpful contributions. I'd also like to extend my gratitude to Yachay Tech for having a different vision of the University in Ecuador focused on the investigation. Finally, I'd like to recognize the assistance of the persons behind the administration and maintenance of the CEDIA HPC, without them this project could never have been finished.

Abstract

Ecuador has several seismicity sources, including the Nazca – South America megathrust in the west, the Interandean Fault System (IFS) between the Cordilleras Occidental and Real, and an active back-arc fold and thrust belt in the East. The surface deformation associated with the subduction megathrust has been well constrained in prior studies, but this is not the case for the other two systems, representing a significant gap in the characterization of seismic hazards. The IFS runs directly under or close to several major cities, including Quito, Riobamba, and Ibarra. Earthquakes have destroyed all these cities in the past. Near Quito, the IFS has a fault called the Quito Fault, which is a thrust fault that underlies and uplifts the city.

This study performs Interferometric Synthetic Aperture Radar (InSAR). InSAR is a tool to characterize the deformation caused by different sources, including faults and landslides using Synthetic Aperture Radar (SAR) images. The processing used in this project will use 280 Sentinel-1 images taken over the area of Quito and the valleys to its east. Then, we use time-series analysis to obtain deformation rates. Moreover, we addressed the main methodological aspects of the processing steps and their implications. The processing of the data collected of Sentinel-1 is an expensive task, so we need to use a High-Performance Computing (HPC) system and different computational techniques for spaceborne geodetic data to process all the data collected in this project.

In general, our results contribute to having a better understanding of seismic hazards in Ecuador. The overarching goal of this work is to develop a deformation map constructed by the deformation caused by the Quito Fault and other sources.

Keywords: InSAR, SAR processing, SBAS, ISBAS, Ecuador

Resumen

En Ecuador existen varias fuentes de sismicidad, estas incluyen la mega falla Nazca-Sudamericana en el oeste, el Sistema de Fallas Interandinas (SFI) entre las Cordilleras Occidental y Real, y un cinturón de pliegues y fracturas del arco posterior activo en el este. La deformación superficial asociada a la mega falla de subducción ha sido bien delimitada en estudios anteriores, pero no es el caso de los otros dos sistemas, lo que representa un vacío importante en la caracterización de los riesgos sísmicos. El SFI pasa directamente por debajo o cerca de varias ciudades importantes, como Quito, Riobamba e Ibarra. Los terremotos han destruido todas estas ciudades en el pasado. Cerca de Quito, el IFS tiene una falla llamada Falla de Quito, que es una falla de empuje que subyace y eleva la ciudad.

Este estudio usa la técnica del Radar de Apertura Sintética Interferométrica (InSAR). InSAR es una herramienta que permite caracterizar la deformación causada por diferentes fuentes, incluyendo fallas y deslizamientos, utilizando imágenes de Radar de Apertura Sintética (SAR). Para el desarrollo de este proyecto se utilizará 280 imágenes del satélite Sentinel-1 tomadas sobre la zona de Quito y los valles del este. A continuación, utilizaremos un análisis de series temporales para obtener los índices de deformación. Además, abordaremos los principales aspectos metodológicos de los pasos de procesamiento y sus implicaciones. El procesamiento de los datos recogidos de Sentinel-1 es una tarea costosa, por lo que necesitamos utilizar un sistema de computación de alto rendimiento (HPC, por sus siglas en Inglés) y diferentes técnicas computacionales para datos geodésicos espaciales para procesar todos los datos recogidos en este proyecto.

En general esperamos que nuestros resultados contribuyen a tener una mejor comprensión de los riesgos sísmicos en Ecuador mediante la creación de mapas de deformación.

Palabras Clave: InSAR, SAR processing, SBAS, ISBAS, Ecuador

Contents

Dedication	v
Acknowledgments	vii
Abstract	ix
Resumen	xi
Contents	xiii
List of Tables	xvii
List of Figures	xix
1 Introduction	1
1.1 Background	1
1.2 Tectonic Setting	3
1.3 Problem Statement	3
1.4 Objectives	4
1.4.1 General Objective	4
1.4.2 Specific Objectives	4
2 Theoretical Framework	7
2.1 Synthetic Aperture Radar	7
2.1.1 Resolution of a SAR system	8
2.1.2 SAR types	9
2.2 SAR interferometry	9
2.2.1 Interferometric coherence	11

2.2.1.1	Phase noise due to temporal change of the scatterers . . .	12
2.2.1.2	Phase noise due to different look	12
2.2.1.3	Phase noise due to volume scattering	13
2.2.2	Unwrapping	13
2.3	Time Series	14
2.3.1	Small Baseline Subset	15
2.3.2	Intermittent Small Baseline Subset	18
3	State of the Art	19
3.1	SBAS Parallel Processing	19
3.1.1	Process-Level Parallelization	20
3.1.1.1	Pleasingly Parallel Processing Steps	20
3.1.1.2	Medium-Grained Data Parallelism	21
3.1.1.3	Coarse-Grained Parallelism by Functional Decoupling . . .	21
3.1.2	Thread-Level Parallelization	22
3.2	Software for processing	22
3.2.1	Sentinel Application Platform (SNAP)	22
3.2.2	GMT and GMTSAR	23
4	Methodology	25
4.1	Data	25
4.2	Sentinel 1 Data	26
4.3	Experimental Environment	26
4.4	Interferogram Generation	27
4.4.1	Processing Flow	27
4.5	Time Series Calculation	30
4.5.1	SBAS approach	30
4.5.2	ISBAS approach	31
5	Results	35
5.1	SBAS results	35
5.2	ISBAS results	37

6	Discussion	39
6.1	Technical Constrains	39
6.1.1	Storage	39
6.1.2	RAM and processing time	40
6.1.3	Data	40
6.2	Malchingui and San Miguel del Comun	41
6.3	San Antonio de Quito	41
6.4	Iñaquito parish of Quito	42
6.5	Solanda neighborhood	43
6.6	Pucará neighborhood	43
6.7	Deformation over Quito	44
7	Conclusions	47
7.1	Conclusions	47
7.2	Future Work	48
	Bibliography	51
	Appendices	59

List of Tables

2.1	Synthetic Aperture Radar types according to the transmitted frequency. . .	9
4.1	Number of interferograms used to generate the time series with the SBAS algorithm grouped by year.	31
5.1	Maximum and Minimum values and its locations, Mean and Standard Deviation values calculated of the Mean LOS velocity from SBAS on each subset of interferograms.	35
5.2	Experiments realized to test the ISBAS method.	37

List of Figures

1.1	Central and South American sites investigated with InSAR and related techniques between 1996 and 2020. Adapted from [1]	2
1.2	Historic earthquakes in the Interandean Valley and Cordillera (blue circles, scaled by magnitude). Figure adapted from [2]. The blue box highlights the study area.	5
1.3	The best-characterized fault segments from [3] based on geologic data, earthquake epicenters, focal mechanisms, and GPS results. While this characterization is adequate for a national hazard study, these faults are not constrained well enough for local hazard assessments. NAS, North Andean Sliver; SOAM, South American plate; INCA, Inca sliver; red star, Quito; blue box highlights the study area.	6
2.1	A SAR system from a satellite. Adapted from [4].	8
2.2	Geometric parameters of a satellite interferometric SAR system. Adapted from [4]	10
2.3	Mono-dimensional phase unwrapping. Adapted form [4]	14
2.4	Example of one obtained interferogram between images obtained on 2020-03-09 and 2020-03-15. (Top) interferogram with wrapped phase with range between $-\pi$ to π . (Bottom) unwrapped solution rewrapped modulo 10 rad (1.59 cycles) for display.	15

3.1	P-SBAS workflow. Black/single and red/multilayered blocks represent sequential and parallel (from a process-level perspective) processing steps, respectively. This scheme reduces to the SBAS sequential workflow when only one processor is employed. From [5].	20
4.1	Methodology to create interferograms	28
4.2	Distribution of the used SAR dataset in the temporal (x-axis) and perpendicular baseline (y-axis) plane where the 'master' or 'reference' is located with baseline = 0 which needs to be central in the baseline plot between all the images. This plot helps us as a reference to create different lists of interferograms by connecting pairs of images.	29
4.3	Interferograms used to generate the time series using SBAS. Yellow: interferograms generated in 2017. Red: interferograms generated in 2018. Blue: interferograms generated in 2019-2020, the data from 2015 and 2016 were discarded due to the data acquisition was more sparse and with larger baseline.	32
4.4	Interferograms used to generate the time series using ISBAS. a) 169 generated with a maximum time span of 12 days, b) 269 generated with a maximum time span of 18 days, and c) 372 generated with a maximum time span of 24 days.	33
5.1	Mean Line-of-sight velocities for three time periods, 2017 (top), 2018 (middle), and 2019-2020 (bottom) using SBAS. Two areas of possible active landslides near the Quito Metropolitan Area are shown (Malchingui, yellow box; San Miguel del Comun, blue box). All rates calculated are relative and the zero value is arbitrary.	36
5.2	Mean Line-of-sight velocities map for the years 2015 to 2020 generated using ISBAS. Red markers are the areas of interest that we discussed in Chapter 6. 1=San Antonio de Quito, 2=Iñaquito parish, 3=Solanda neighborhood, and 4= Pucará neighborhood. The white shaded area was used to create figure 6.5	38

6.1 Left: Mean Line-of-sight velocities in the area near the Rosita quarry in San Antonio of Pichincha delimited by the polygon $-78.4312/-78.4211/0.0333/0.0394$ (min longitude/max longitude/min latitude/max latitude). Right: Time series of the accumulated displacement in the period between 2015 to 2020 in the location $-78.4276/0.0351$ (lon/lat) indicated by the black star in the left figure. The time series shows one large jump on (date) that is related to an unwrapping error in a single interferogram, rather than a real ground displacement. 42

6.2 Left: Mean Line-of-sight velocities in the Iñaquito parish of Quito near to the Carolina Park delimited by the polygon $-78.4854/-78.4751/-0.1773/-0.1673$ (min longitude/max longitude/min latitude/max latitude). Right: Time series of the accumulated displacement in the period between 2015 to 2020 in the location $-78.4812/-0.1725$ (lon/lat) remarked in the black star in the left figure. 43

6.3 Left: Mean Line-of-sight velocities in the south of Quito at the Solanda neighborhood delimited by the polygon $-78.5479/-78.5376/-0.2765/-0.2673$ (min longitude/max longitude/min latitude/max latitude). Right: Time series of the accumulated displacement in the period between 2015 to 2020 in the location $-78.5416/-0.2711$ (lon/lat) indicated by the black star in the left figure. 44

6.4 Left: Mean Line-of-sight velocities in the south of Quito at the Pucará neighborhood delimited by the polygon $-78.5401/-78.5293/-0.3423/-0.3315$ (min longitude/max longitude/min latitude/max latitude). Right: Time series of the accumulated displacement in the period between 2015 to 2020 in the location $-78.53407/-0.3386$ (lon/lat) indicated by the black star in the left figure. 44

6.5 Distribution of the mean LOS velocities as a function of latitude for a bin approximately 30 km wide, centered on Quito. The green line represents a smoothed mean velocity of the latitude points. 45

Chapter 1

Introduction

1.1 Background

Interferometric Synthetic Aperture RADAR (InSAR) measures the phase difference between two Synthetic Aperture RADAR (SAR) images at different times from the same orbital position [1]. There are several satellites that can produce these images such as Sentinel, Envisat and ALOS that will be described later in more detail. The result of this operation is known as an interferogram. It provides a unique tool for the quantitative measurement of the surface deformation of the Earth produced by natural and non-natural processes [6].

Over time many measurement techniques have been developed to study the Earth's surface deformation, for example, the space-geodetic and the InSAR techniques. These techniques offered new opportunities for precise deformation monitoring in geomatics engineering [7].

In [1], researchers constructed a literature review to determine all the applications of InSAR in Central and South America. Figure 1.1 shows the applications and the area of investigation. They classified the range of applications into seven categories according to the study object: earthquakes, volcanoes, ice, subsidence and mining, landslides, and wetland InSAR. In Ecuador, the principal applications are on earthquakes and volcanoes.

Volcanoes are the most monitored surfaces in Ecuador. The Tungurahua volcano was studied in [8] and [9]; the authors created 13 interferograms to detect any deformation between periods of activity in 1994, 1998, and 1999. Recently, [10] studied its activity



Figure 1.1: Central and South American sites investigated with InSAR and related techniques between 1996 and 2020. Adapted from [1]

between July 2003 and June 2009 using 22 Envisat images. A large study over volcanoes of Colombia, Ecuador, and Peru was done by [11] using 465 ascending SAR scenes for 27 frames acquired between the end of 2006 and the beginning of 2011 by the ALOS satellite, the Ecuadorian volcanoes studied were Sangay, Tungurahua, Guagua Pichincha, and Reventador. These studies provided a high-density map of measurements, in order to constrain the magma plumbing system during pre-eruptive, co-eruptive, post-eruptive deformation. Other studies on Ecuadorian volcanoes are described in [12] and [13].

Earthquakes are the other events studied in Ecuador. Recently, the Pedernales earthquake which occurred on 16 April 2016 has been studied in [14, 15, 16] using the data of Sentinel 1-A and ALOS-2 satellites. The results shows an elliptical fringe pattern with a maximum 65 cm ground motion away from the satellite, consistent with subsidence and trench ward horizontal motion above the base of the rupture zone. In addition, another surface faulting event that occurred in the Pisayambo area on 26 March 2010 was studied in [17].

Ecuador is located in a tectonically active zone with several sources of seismic hazard that are not well defined. In particular, active faults in the Interandean Valley are challenging to locate in the field due to extensive volcanic cover. This is a pressing concern since the valley is home to about half of the population of Ecuador.

We perform InSAR processing of data from Sentinel-1 in the dry Interandean Valley to generate a large set of interferograms, contribute to the characterization of the Quito Fault, and measure the surface deformation over the area of Quito (See Fig. 1.3).

1.2 Tectonic Setting

Ecuador is sliced by multiple large fault systems, which include the offshore subduction zone megathrust between the South American and Nazca plates, a back-arc fold and thrust belt (eastern sub-Andean belt), and an intra-arc complex fault system, known as the Cosanga-Chingual-Pallatanga-Puna fault system (CCPP), see Fig. 1.3. The latter accommodates the northward motion of the North Andean Sliver and has been host to many damaging earthquakes over the last few hundred years [2], see Fig. 1.2. The location of the CCPP coincides with the inter-Andean Valley, which is home to approximately 60% of the population of Ecuador, representing a source of seismic hazard.

With increasing data, such as geologic observations, better earthquake locations, and GPS, these systems are becoming better known, see Fig. 1.3. However, a challenging landscape that includes 80+ active volcanoes, rapid erosion due to the uplifting mountains, dense vegetation areas and precipitation means the exact locations and movement rates are often unquantified. Only the Pallatanga segment of the CCPP has been thoroughly characterized from a paleoseismological perspective [18]. In this study, we aim to better characterize the urban area of Quito, which runs near the Quito Fault System, and to identify other unknown fault segments that may affect the Ecuadorean Andes, given the poor characterization thus far.

1.3 Problem Statement

As it is described in Section 1.1, most InSAR studies realized in Ecuador have been applied on areas over volcano and earthquakes epicenters without an analysis of deformation over

the years. The studies that created a time series analysis on the area of the metropolitan area of Quito were done in [19] by using 19 European Remote Sensing (ERS) acquisitions collected in descending mode between May 1993 and September 2000, and in [20] by using 105 images acquired in descending mode between October 2014 and November 2018 from the satellite Sentinel 1.

The increasing of SAR sensors orbiting the Earth has increased the availability of data that can be analyzed. New images arrive every few days, new data processing chains are required to obtain new interferometric results. In addition, ground deformation time-series computation requirements will significantly increase with the availability of new sensors and new images.

1.4 Objectives

1.4.1 General Objective

Construct deformation maps with different InSAR methods by processing an extensive data set of SAR images acquired by the satellite Sentinel 1 with information over the area of Quito.

1.4.2 Specific Objectives

- Generate a large set of interferograms using the data available from the satellite Sentinel 1 and process the generated interferograms to do a multi-temporal InSAR analysis.
- Adopt suitable computational methods to perform the computationally intensive processing stages of the SAR interferometric processing by exploiting the capabilities of High-performance computing (HPC) systems.
- Take into account the temporal relationships among long-term sequences of SAR acquisitions and obtain the evidence of the ground surface changes over time caused by human activities or natural hazards.

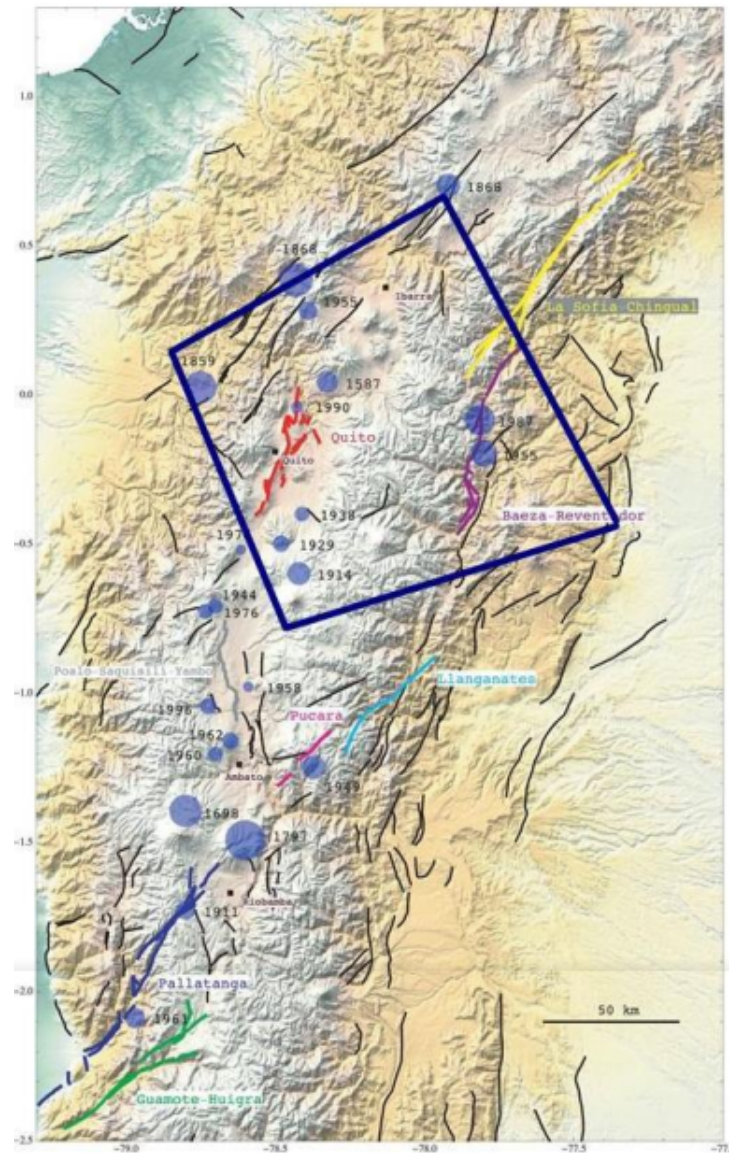


Figure 1.2: Historic earthquakes in the Interandean Valley and Cordillera (blue circles, scaled by magnitude). Figure adapted from [2]. The blue box highlights the study area.

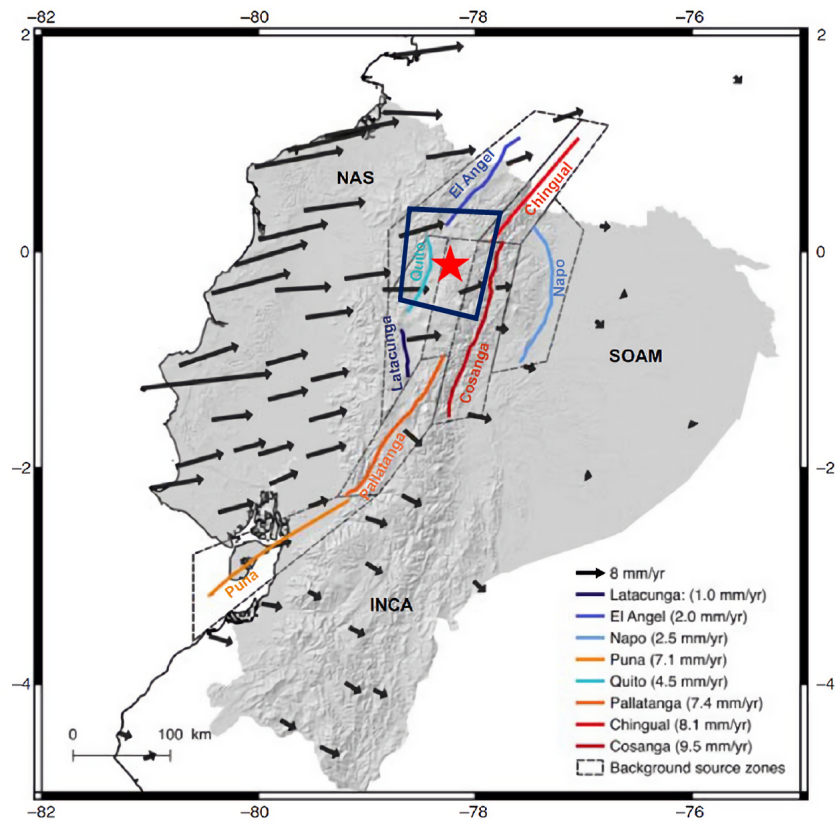


Figure 1.3: The best-characterized fault segments from [3] based on geologic data, earthquake epicenters, focal mechanisms, and GPS results. While this characterization is adequate for a national hazard study, these faults are not constrained well enough for local hazard assessments. NAS, North Andean Sliver; SOAM, South American plate; INCA, Inca sliver; red star, Quito; blue box highlights the study area.

Chapter 2

Theoretical Framework

This chapter introduces the fundamental principles for following this research. First, we will review the concept of Synthetic Aperture Radar; then, we will address the theory behind SAR interferometry, followed by its limitations; finally, we describe the methods for creating time series.

2.1 Synthetic Aperture Radar

Synthetic Aperture Radar (SAR) is a coherent, active microwave remote sensing instrument, which is known due to its capability to efficiently map the scattering properties of the Earth's surface [6]. The SAR sensor is mounted on an aircraft or satellite. It is a form of radar that can create two-dimensional or three-dimensional image reconstructions of objects. This technique implies a projection from the three-dimensional object space to a planar two-dimensional radar image.

The radar system transmits electromagnetic pulses with high power and receives the echoes of the backscattered signal sequentially. Typical values for the pulse repetition frequency range from a few hundred to a few thousand Hertz for airborne and spaceborne systems, respectively [21]. The radiation transmitted from the radar has to reach the scatterers on the ground and then come back to the radar in order to form the SAR image (two-way travel)[4].

SAR is an active imaging sensor; it works without the need for an external energy source. Moreover, since it typically operates in the microwave region of the electromagnetic spectrum, it can be used efficiently in any meteorological condition and with a complete

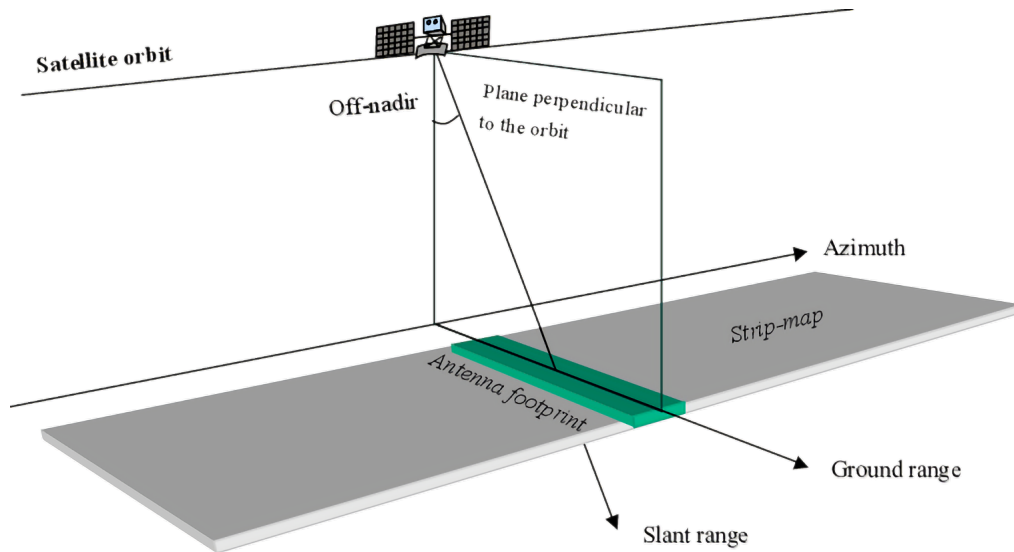


Figure 2.1: A SAR system from a satellite. Adapted from [4].

day-and-night operational capability [6].

A digital SAR image is seen as a two-dimensional array formed by columns and rows containing small picture elements (pixels). Each pixel is associated with a small region of the Earth's surface called a resolution cell. It contains a complex number that provides amplitude and phase information concerning the microwave field backscattered by all the scatterers (rocks, vegetation, buildings, others.) within the corresponding resolution cell projected on the ground [4]. See the geometry of a SAR antenna in Figure 2.1, where the direction along the slant-range direction is usually called the Line of Sight (LOS).

2.1.1 Resolution of a SAR system

The location and dimension of the resolution cell in azimuth and slant-range coordinates depend only on the SAR system characteristics [4]. When we refer to the resolution of an image, we should treat it as Range resolution and Azimuth resolution, (see fig. 2.1).

- **Range Resolution:** refers to the across-track dimension perpendicular to the flight direction.
- **Azimuth Resolution:** refers to the along-track dimension parallel to the flight direction.

2.1.2 SAR types

Depending on the frequency band, considerable penetration can occur so that the imaged objects and media must be modeled as a volume (e.g., vegetation, ice, snow, dry soil). More penetration of the electromagnetic pulses in media will occur for radar systems using longer wavelengths which usually have an accentuated volume contribution in the backscattered signal [21]. Different frequency bands are shown in table 2.1.

Table 2.1: Synthetic Aperture Radar types according to the transmitted frequency.

Frequency Band	Frequency [GHz]	Wavelength [cm]	Antenna
Ka	40–25	0.75–1.2	Astra 3B
Ku	17.6–12	1.7–2.5	Astra 3B
X	12–7.5	2.5–4	Kompsat-5, PAZ
C	7.5–3.75	4–8	Sentinel-1a/1b
S	3.75–2	8–15	HJ-1C
L	2–1	15–30	ALOS/PALSAR, ALOS-2
P	0.5–0.25	60–120	BIOMASS (2023)

The most common uses of SAR antennas vary according to the wavelength, and the frequency bands are: The P and L bands are used in biomass estimation, subsurface imaging, and foliage penetration. The L, C, S, and X bands are used in agriculture and subsidence monitoring. The X and Ku bands are used for snow monitoring. Finally, the X and Ka bands are used for high-resolution imaging [21].

2.2 SAR interferometry

Each SAR image pixel phase contains information that is accurate to a small fraction of the radar wavelength. It is possible to detect and measure tiny path length differences with centimetric or even millimetric accuracy [21].

A satellite SAR can observe the same area from slightly different look angles. The inclination of the antenna with respect to the nadir is called the off-nadir angle. The distance between the two satellites (or orbits) in the plane perpendicular to the orbit is called the interferometer baseline, and its projection perpendicular to the slant range is the perpendicular baseline [4], see Fig. 2.2.

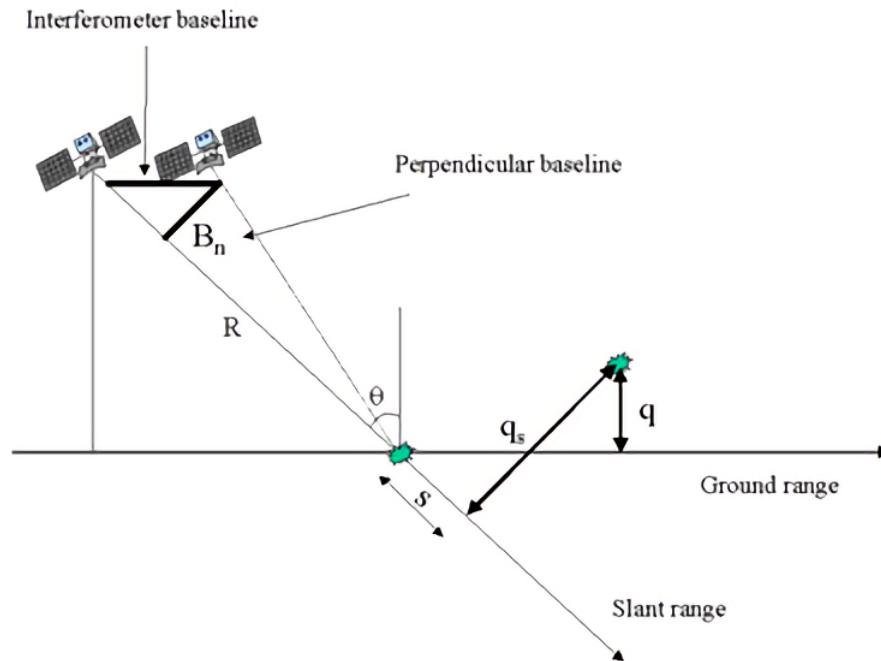


Figure 2.2: Geometric parameters of a satellite interferometric SAR system. Adapted from [4]

Because satellites travel in predictable and repeatable orbits, SAR images are obtained for nearly the exact location. The interferogram between two of these images provides quantitative measures of the changes in elevation of the surface. Mathematically, an interferogram takes in the following parameters:

- The perpendicular baseline to the line of sight (LOS) B_n .
- The radar-target distance R .
- The displacement between the resolution cells along the perpendicular to the slant range, q_s .
- The wavelength of the radar λ .

The interferometric phase variation is computed in [22], where both SAR images are composed of a regular grid with complex values, v_1 and v_2 , they are decomposed in a phase and an amplitude component as follows:

$$\begin{aligned} v_1 &= |v_1|e^{j\psi_1}, \\ v_2 &= |v_2|e^{j\psi_2}. \end{aligned} \tag{2.1}$$

Where ψ_1 and ψ_2 represents the observed phase. These values in the two images for the resolution cell M are:

$$\begin{aligned} \psi_{1M} &= -\frac{2\pi 2R_1}{\lambda} + \psi_{scat,1M}, \\ \psi_{2M} &= -\frac{2\pi 2R_2}{\lambda} + \psi_{scat,2M}, \end{aligned} \tag{2.2}$$

where $\psi_{scat,1M}$ and $\psi_{scat,2M}$ are the noise contributions to the phases of both images, and R_1 and R_2 are the geometric distances. In this case, we are ignoring the phase contributions due to the noise produced by the signal propagation delay. These characteristics are equal on both acquisitions, $\psi_{scat,1M} = \psi_{scat,2M}$.

Then, after aligning and re-sampling the v_2 grid to the corresponding location of v_1 , the complex interferogram is generated by the complex multiplication:

$$v = v_1 v_2^* = |v_1||v_2|e^{j(\psi_1 - \psi_2)} \tag{2.3}$$

The interferometric phase can be written as:

$$\phi_M = (\psi_1 - \psi_2) = -\frac{4\pi(R_1 - R_2)}{\lambda} = -\frac{4\pi\Delta R}{\lambda}. \tag{2.4}$$

where ΔR is the variation of the travel path difference and is determined by $\Delta R = -2\frac{B_n q_s}{R}$ [4].

Fig. 2.4 shows an example of the phase differences obtained for a pair of SAR images acquired by the Sentinel 1 SAR satellite of the European Space Agency.

2.2.1 Interferometric coherence

InSAR techniques work under coherent conditions; the pulses received need to be correlated between both SAR acquisitions. In an interferometric application, spatial coherence is the most important to consider. Coherent radar echoes, that is, those with measurable phase and amplitude, will be correlated with each other if each represents nearly the same interaction with a scatterer or set of scatterers [23].

The loss of coherence is known as decorrelation and, it can be defined as the presence of noise in the interferogram phase. The complex coherence of two zero-mean complex signals v_1 and v_2 is defined in [24] as:

$$\gamma = \frac{\left| \sum_{n=1}^N v_1^{(n)} v_2^{*(n)} \right|}{\sqrt{\sum_{n=1}^N |v_1^{(n)}|^2 \sum_{n=1}^N |v_2^{(n)}|^2}}. \quad (2.5)$$

When the two radar images are precisely the same, correlation equals one, and when they are entirely different, the correlation approaches zero [25]. Three main contributions to the phase noise that should be taken into consideration are caused due to temporal change of the scatterers, different look angles, and volume scattering.

2.2.1.1 Phase noise due to temporal change of the scatterers

In a water basin or densely vegetated areas, the scatterers change totally after a few milliseconds, whereas exposed rocks or urban areas remain stable even after years. Of course, there are also intermediate situations where the interferometric phase is still valid even if corrupted by change noise [4]. Temporal decorrelation is one of the principal constraints of InSAR technology and especially over vegetated regions, where decorrelation rises with the amount of vegetation cover because the scatterers of the plants sensibly change over time [25]. It is more significant at the lower frequencies (C-band) than at the higher frequencies (L-band). For this reason, the use of L-band SAR data, provided (for instance) by the ALOS-1/2 Japanese RADAR instrument, is advantageous for the monitoring of surface height and the changes over time of terrain covered by vegetation [6].

2.2.1.2 Phase noise due to different look

The consequence of the different look angle influence is a critical baseline over which the interferometric phase is complete noise. The critical baseline depends on the ground range resolution cell (and thus, the terrain slope), radar frequency, and sensor-target distance. This phase noise term, however, can be removed from the interferogram employing a pre-processing step of the two SAR images known as spectral shift or standard band filtering [4].

2.2.1.3 Phase noise due to volume scattering

The critical baseline reduces in the case of volume scattering when the elementary scatterers are not disposed on a plane surface but occupy a volume [4].

Several noise-filtering methods have been developed over the last three decades to reduce the decorrelation noise in single InSAR interferograms [26, 27, 28]. Recently, new hybrid multi-temporal InSAR noise-filtering approaches have also been proposed [6].

2.2.2 Unwrapping

One of the most complex and essential steps in the analysis of InSAR data is the extraction of the absolute phases from the available wrapped values [29]. This step is called two-dimensional phase unwrapping. Phase can be measured only modulo 2π , so physical quantities derived from interferometric phase data are wrapped with respect to some modulus or ambiguity and must be unwrapped to provide meaningful information [30]. The two-way interferometric phase is always between 0 and 2π , representing in the case of Sentinel 1 a maximum path-length difference of 2.77 cm, half the satellite wavelength of 5.55 cm. Unwrapping is the process of adding the correct integer multiples of 2π to the interferometric fringes to resolve the phase discontinuities [4]. This problem was proved as an *NP-hard* (a problem that complexity theory suggests is impossible for efficient algorithms to solve exactly since it is a special case of the minimum concave cost network flow problem.) [31].

However, deformation in the area of interest and atmospheric noise caused by tropospheric and ionospheric effects can give rise to multiple phase cycles. A solution for this problem was proposed in [29, 30, 31] and, it is an excellent technique to measure the surface topography, deformation, or velocity. The generation of Digital Elevation Models (DEM) is one of its applications. The DEM is used to apply topographic corrections.

The 1-D case has the effect of returning a wrapped phase signal to a continuous phase signal that is free from 2π jumps as it is explained in Figure 2.3. Figure 2.4 shows an example of a two-dimensional case: a wrapped interferogram and an unwrapped interferogram.

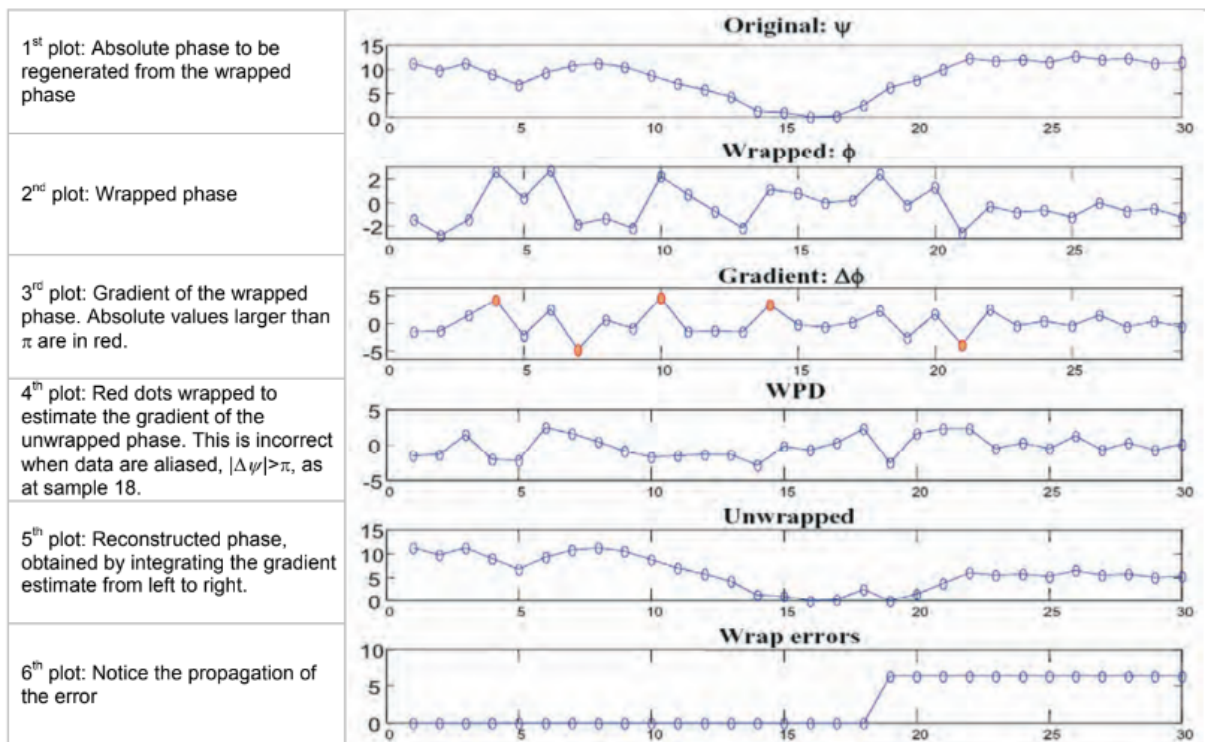


Figure 2.3: Mono-dimensional phase unwrapping. Adapted from [4]

2.3 Time Series

The InSAR applications are not only used to monitor deformation events on specific dates. Likewise, they are used to analyze the temporal deformation of prolonged events such as time series. The time series are created using more than two SAR images [6, 32, 33].

The InSAR technology plays an essential role in surface displacement analysis and monitoring. However, we must remark that it also has critical limitations, the most relevant being those due to the noise effects on the interferograms known as the decorrelation phenomena. These phenomena are solved by the creation of time series [34]. During the last three decades, there were developed two groups of algorithms, the Small Baseline Subset method [32], and the Permanent Scatterers [33]. The principal difference between both methods is the criteria for pairing the SAR images to create the interferograms.

In this study, we are going to use the SBAS method [32], and an approach based on it called Intermittent SBAS [35].

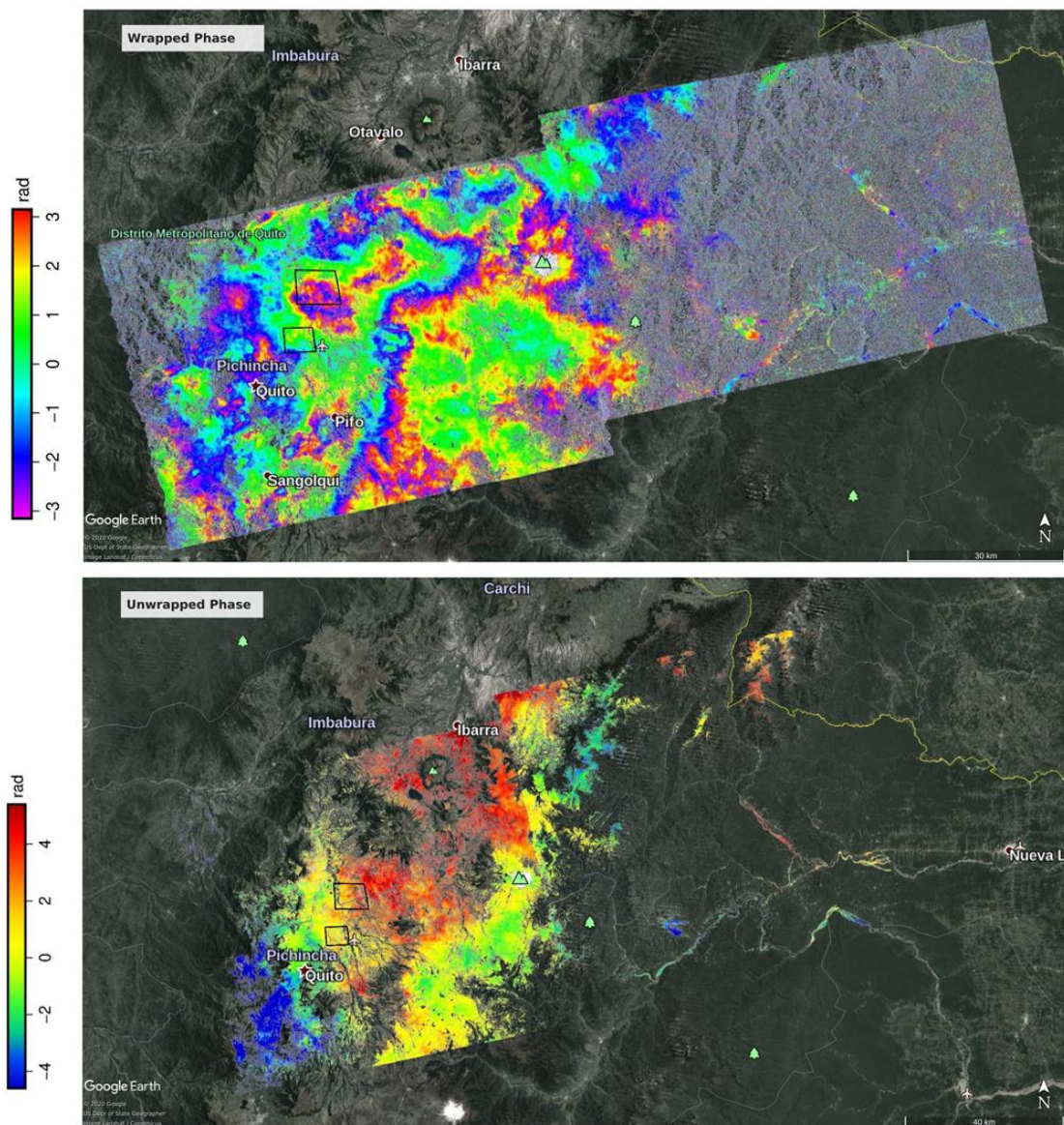


Figure 2.4: Example of one obtained interferogram between images obtained on 2020–03–09 and 2020–03–15. (Top) interferogram with wrapped phase with range between $-\pi$ to π . (Bottom) unwrapped solution rewrapped modulo 10 rad (1.59 cycles) for display.

2.3.1 Small Baseline Subset

The SBAS procedure allows us to produce mean deformation velocity maps and deformation time series for each coherent pixel of an investigated area [32]. Since its development, it has provided the capability to detect and investigate deformation phenomena; and, it has been already shown in different applications, primarily based on exploiting the European Remote Sensing (ERS) SAR data, acquired in C-Band [34].

The main idea of SBAS is to select the interferometric pairs guided by the need to preserve the Spatio-temporal correlation [5]. It can be achieved by setting a maximum threshold of spatial and temporal separation, which means that the generated interferograms are characterized by a small spatial and temporal baseline and, as well, by a minor frequency. As a consequence of these limitations, the SAR images associated with the interferograms generation could be grouped in several independent small baseline subsets that must be linked appropriately in order to retrieve the deformation time series [34]. A detailed discussion on the SBAS approach is clearly outside the scope of this work and can be found in [32].

The generation of a number M of interferograms represents the starting point of the proposed technique, involving a set of $N + 1$ SAR images relative to the same area and acquired at the ordered times (t_0, \dots, t_N) . We assume that the phase signal of each unwrapped interferogram is referenced to a pixel characterized by high coherence, whose deformation behaviour is located in a non-deforming zone.

Now, refer to a generic pixel of our SAR images with azimuth and range coordinates $(x; r)$. The expression for the j -interferogram computed from the SAR acquisitions at times t_A and t_B according to [32] is:

$$\begin{aligned} \delta\phi_j(x, r) &= \phi(t_B, x, r) - \phi(t_A, x, r) \\ &\approx \frac{4\pi}{\lambda} [d(t_B, x, r) - d(t_A, x, r)] + \frac{4\pi}{\lambda} \frac{B_{\perp j} \Delta z}{r \sin \theta} \\ &\quad + \frac{4\pi}{\lambda} [d_{atm}(t_B, x, r) - d_{atm}(t_A, x, r)] + \Delta n_j, \forall j = 1, \dots, M, \end{aligned} \quad (2.6)$$

where $\phi(t_B, x, r)$ and $\phi(t_A, x, r)$ represent the phases of the two images involved in the interferogram generation. The first term represented by $d_B(t_B, x, r)$ and $d_A(t_A, x, r)$ are the radar line of sight projections of the cumulative deformation at times t_A and t_b , with reference to the acquisition time t_p , this implies that $\phi(t_0, x, r) = 0, \forall(x, r)$. The second term accounts for possible topographic artifacts Δz that can be present in the DEM; it depends on the perpendicular baseline component $B_{\perp j}$, the sensor-target distance r and the look angle θ . The terms $d_{atm}(t_B, x, r)$ and $d_{atm}(t_A, x, r)$ accounts for possible atmospheric phase artifacts and the last term Δn_j for the decorrelation phenomena and by the thermal noise effects.

With expression in 2.6, we can define the following system of equations M in unknowns N as the following matrix representation:

$$A\phi = \delta\phi, \quad (2.7)$$

where ϕ is the vector of N unknown phase values associated with the deformation of the considered pixel, $\phi^T = [\phi(t_0), \dots, \phi(t_N)]$. The vector $\delta\phi$ consists of the M known values of the pixel computed by the interferograms, $\delta\phi^T = \delta\phi_1, \dots, \delta\phi_M$. The matrix A is a $M \times N$ matrix that directly depends on the set of interferograms generated from the available data. Note that the SBAS technique implies a pixel-by-pixel temporal analysis.

The equation system in (2.7) can be modified in such a way as to replace the unknowns with the mean phase velocity between time-adjacent acquisitions and the new unknowns become:

$$v^T = \left[v_1 = \frac{\phi_1}{t_1 - t_0}, \dots, v_N = \frac{\phi_N - \phi_{N-1}}{t_N - t_{N-1}} \right]. \quad (2.8)$$

and, we get a new system of equations represented by:

$$Bv = \delta\phi, \quad (2.9)$$

wherein B represents an $M \times N$ matrix whose expression can be found in [32].

A simple solution for inverting the system in 2.9 is provided by the Singular Value Decomposition (SVD) method. This method allows us to evaluate the pseudo-inverse of the matrix B . The velocity vector v allows us to mitigate the presence of significant discontinuities in the final result [34]. Finally, an additional integration step is necessary to compute the solution ϕ from the estimated vector v .

To summarize, the SBAS procedure allows us to satisfy two essential requirements: maintain the capability of the system to provide spatially dense deformation maps by employing SAR data pairs with small baseline values, and maximize the temporal sampling rate of the retrieved displacements signals by employing almost all the usable SAR acquisitions.

Consequently, the SBAS approach permits us to detect and follow the temporal evolution of surface deformation with a high degree of temporal and spatial coverage using a set of interferograms.

2.3.2 Intermittent Small Baseline Subset

The Intermittent Small Baseline Subset algorithm described in [35] is based upon the SBAS method that uses low-resolution, multi-looked interferograms that are individually phase unwrapped. This method considers each interferogram separately, selecting and unwrapping pixels with high coherence in that layer only. This method aims to adapt SBAS to use the intermittent coherence of areas to expand the number and distribution of point areas of ground deformation. It works as follow:

Let (x, r) be the row and column coordinates and j be the j th interferogram, there are specific conditions on the selection of points (x, r) and layers (j) . For any (x, r) , only those layers, j , for which there exists an unwrapped phase (pixels with high coherence) are used. The number used, t , will differ from point to point. Furthermore, only those point coordinates (x, r) for which $t > T$, where T is a threshold based on a specific number of coherent interferograms, are used in the analysis. The value of the threshold T selected is based on two criteria: maximizing T to reduce uncertainty in the solution and minimizing T to increase the spatial distribution of points. The final selection of the threshold is a trade-off between these two properties.

A solution that closely matches the SBAS solution would be to set T as a large number close to the number of interferograms available. However, it is unlikely since it would result in any improvement in the number and distribution of points, and therefore smaller values of T are considered.

Chapter 3

State of the Art

Researchers developed advances in ground deformation time-series computation in recent years. The recent advances are focused on adopting suitable computational methods for generating and processing large data sets of interferograms [1]. The first section of this chapter will describe a processing chain for processing a large group of interferograms. The second one describes a project that exploits the capabilities of a High-Performance Computing architecture to provide interferometric products. Finally, the last section will explain the software used to perform this processing.

3.1 SBAS Parallel Processing

The sequential implementation of the SBAS processing chain could be computationally expensive when a large data set is processed. Specifically, the processing time of the SBAS chain may be a limitation in case of emergency response situations or monitoring contexts. Subsequently, results are required to be available in a short time [36].

The methodology proposed in [37] presents a parallel computing solution for the SBAS processing chain, referred to as P-SBAS, which is particularly appropriate to exploit the current available parallel hierarchal structures. This methodology has to lead the development of different researches that focus on the processing of large SAR data sets such as in [36, 38, 39, 40], and others. The advantage of parallel hierarchal platforms is applying a dual-level parallelization strategy proposed as the process and the thread-level. The algorithmic composition of the particular processing step (e.g., raw data focusing, image co-registration, phase unwrapping) is essential to classify them according to a paralleliza-

tion strategy.

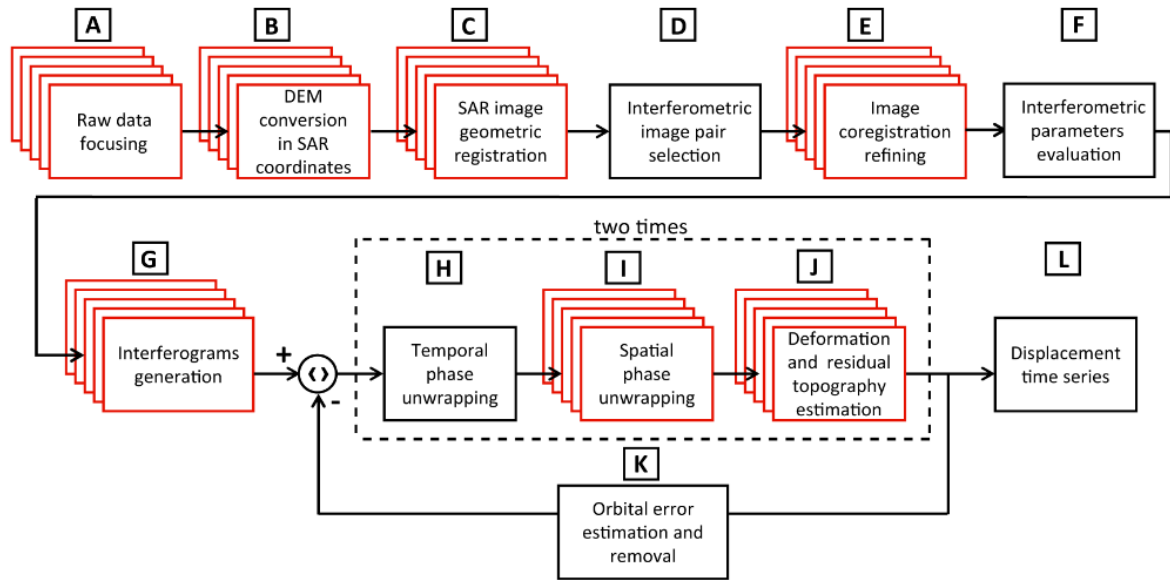


Figure 3.1: P-SBAS workflow. Black/single and red/multilayered blocks represent sequential and parallel (from a process-level perspective) processing steps, respectively. This scheme reduces to the SBAS sequential workflow when only one processor is employed. From [5].

3.1.1 Process-Level Parallelization

Multiprocessor systems with distributed memory use this P-SBAS parallelization strategy. Fig. 3.1 presents a synoptic representation of the suggested computational solution. It schematically explains the modular composition related to the process-level parallelism where red sections mean parallel-performed processing stages and black sections refer to non-parallel computations and, different steps involve different parallelization approaches. The three main parallelization strategies are the coarse, medium and granularity-based strategies and are used according to a particular section of the processing chain [37]. We will describe this parallelization strategies:

3.1.1.1 Pleasingly Parallel Processing Steps

This approach suggests a minimal effort to partition the application into independent parallel parts [41]. The processing steps A (raw data focusing), C (SAR image geometric

co-registration), E (image co-registration refining), and G (interferogram generation) of the SBAS elaboration chain (see Fig. 3.1) are desirable stages for being cast here. These elaboration steps work on 2-D data, although the relevant algorithmic structure of the realized functional can be rather complex. For example, raw data focusing (block A) applies to a collection of SAR raw data. It can lead to a set of independent computations by treating independently each elaboration of a single raw data that can naturally be executed concurrently into multiple processors. Similar considerations apply for the subsequent mentioned stages. The benefits in terms of simplicity of realization and reduction of communication costs are evident. The principal disadvantage of this strategy concerns the limited scalability. Nevertheless, such a limitation may be reasonable when a large SAR dataset is considered [37].

3.1.1.2 Medium-Grained Data Parallelism

This approach refers to data manipulation performed in parallel. This parallelism exploits multiple processors that work on different portions of the data [41]. It relies on the fact that the same operation needs to be applied to distinct parts of a large data structure. This kind of parallelization has explicitly been exploited within the elaboration steps B (DEM conversion in SAR coordinates) and J (spatial phase-unwrapping) of the SBAS processing chain (Fig. 3.1), both dealing with the processing of large multidimensional (2-D and 3-D) arrays that can be performed by separately executing the same elaboration on pieces of the input data [37].

3.1.1.3 Coarse-Grained Parallelism by Functional Decoupling

This approach relies on analyzing an ad-hoc strategy for the phase unwrapping problem [42](H and I stages), and its elaboration includes complex computations. It is not generally possible to directly obtain independent calculations that can be solved in parallel. The definition of the logic of this parallelization procedure takes preliminary considerations on the algorithm structure of the optimized sequential version, and the inherent subtle-flow dependencies need to be specified to reduce the solution into a set of independent subproblems. The coarse-grained parallelism is implemented by distributing the individual subproblems to participating processors in a round-robin fashion. In this case, it adopts

static scheduling with minimum communication and synchronization cost [37].

3.1.2 Thread-Level Parallelization

It relies on a fine-grained parallelization and has been implemented just for the most complex computational stages A, H, and I of Fig. 3.1. The phase unwrapping computation and raw data focusing are the most time-consuming calculations. To complement the coarse/medium-grained parallelization adopted in the previous section, it suggested a fine-grained shared-memory parallelization strategy. An exhaustive discussion of the multi-threading parallelization strategy requires a detailed algorithm structure analysis [37].

3.2 Software for processing

Various research groups base their systematic processing approaches on open-source software such as Sentinel Application Platform (SNAP) and the Generic Mapping Tools Synthetic Aperture Radar (GMTSAR) for the generation of differential interferograms [43].

3.2.1 Sentinel Application Platform (SNAP)

Sentinel Application Platform is a well-known architecture for ESA Toolboxes ideal for use for Earth observation data. It is open-source software under the GNU GPL v3 license. The European Space Agency (ESA) supports the project through the Scientific Toolbox Exploitation Platform (STEP). It encourages the scientific exploitation of the ERS-ENVISAT missions, the satellites Sentinels 1,2,3, and several National and Third Party Missions. The three toolboxes are respectively Sentinel 1, 2, and 3 Toolboxes. They contain some functionalities of previous toolboxes that were developed over the last few years [44].

The Sentinel-1 Toolbox (S1TBX) consists of a set of processing tools, data product readers and writers and, a display and analysis application to support the archive of data from ESA SAR missions: ENVISAT, ERS-1 and 2, and SENTINEL-1, as well as other SAR data such as RADARSAT-2, COSMO-SkyMed, TerraSAR-X and, ALOS PALSAR. The multiple processing tools could be integrated within the graphical user interface and run independently from the command line. The Toolbox incorporates tools for calibration, speckle filtering, coregistration, orthorectification, mosaicking, data conversion, polarime-

try and, interferometry [44]. Meanwhile, the Sentinel-2 Toolbox (S2TBX) and Sentinel-3 Toolbox (S3TBX) consists of a rich set of visualisation, analysis and processing tools for the exploitation of Sentinel 2 and Sentinel 3 data respectively [44].

3.2.2 GMT and GMTSAR

The Generic Mapping Tools (GMT) system was launched in 1987 at Lamont-Doherty Earth Observatory of Columbia University and is an open-source software. GMT is a collection of command-line tools for manipulating geographic and Cartesian data sets and producing high-quality illustrations ranging from simple x–y plots via contour maps to artificially illuminated surfaces and 3D perspective views. Its tools include filtering, trend fitting, gridding, projecting, and others. GMT allows users to manipulate 2D and 3D data to generate process data, generate publication-quality illustrations, automate workflows, and make animations.[45]

The software Generic Mapping Tools Synthetic Aperture Radar (GMTSAR) [46] is an open-source InSAR processing system meant for users familiar with GMT. The GMTSAR code is written in the C programming language and supports several fast Fourier transform libraries built-in Fortran. It will run on any computer with the following dependencies: GMT and Network Common Data Format (NetCDF).

The software has three main components:

1. A preprocessor to convert the native satellite format and orbital information into a generic format for the following satellites: ERS-1/2, Sentinel-1A/B, Radarsat-2, TerraSAR-X, COSMOS-SkyMed, ALOS-1, ALOS-2, and Envisat;
2. An InSAR processor to focus and align stacks of images, map topography into phase, and form the complex interferogram; and
3. A postprocessor, mostly based on GMT, with two aims. The first is to filter the interferograms. The second is to construct the interferometric products of phase, coherence, phase gradient, and line-of-sight displacement in radar and geographic coordinates.

Chapter 4

Methodology

This chapter presents the overall methodology that we used in the development of this research; we divided it into five sections: the first two ones describes the data provided by the Sentinel 1 satellite; the third one characterizes the environment used to compute all the data; the fourth describes the process used to generate the interferograms; the last one describes the scheme for calculating the time series.

4.1 Data

The European Space Agency (ESA) obtained the images utilized under the Copernicus Sentinel project; the images were downloaded from the repository of the Alaska Satellite Facility (ASF). We utilized the pictures taken by the satellites Sentinel 1-a and 1-b in ascending orbit on path 120 between -0.3° and 0.4° latitude and, between -78.71° and -77.87° longitude (see Fig. 1.3). We downloaded and processed 280 pictures taken within the north of Ecuador between October 2014 to October 2020.

In addition to the Sentinel Data, the other necessary inputs are a high-resolution Digital Elevation Model (DEM) in GMTSAR-readable format (GMT .grd file) and the orbit files for Sentinel-1. We used the Shuttle Radar Topography Mission (SRTM) 1-arcsecond dataset from NASA for the DEM, corrected to the WGS84 ellipsoid datum by removing the EGM96 geoid model. All these data are freely available. We obtained the orbit files from the ESA. The orbit files are records of the exact position of a SAR satellite in space during the time the image was taken, which is needed for computing topographic effects and geo-coding the data.

4.2 Sentinel 1 Data

Sentinel-1 has been in orbit since April of 2014. It has provided complex images with phase and amplitude information from throughout the world. We will focus on the Quito area since that is a dry zone with low vegetation. These area conditions are ideal for obtaining clear images from Sentinel-1 with low noise, which can be used to detect surface deformation.

Sentinel-1 works with a frequency of 5.405 GHz (C-band). This frequency range typically reflects from the surface and top layer of the forests, making interferometry one of its most popular applications.

The Sentinel 1 satellites provide us the following products:

- *Level 0*: These products contain compressed and unprocessed instrument source packets, with additional annotations and auxiliary information to support processing. They require SAR processing and can be used by scientists testing SAR data processing. The data is provided as XML and TIFF files [47].
- *Level 1*: These products contain focused data. It is the product intended for most data users and is generally available. Level-0 products are processed into a Level-1 product by applying algorithms and calibration data to form a baseline engineering product. We can generate focused Level-1 Single Look Complex (SLC) products and Level-1 Ground Range Detected (GRD) products [47].
- *Level 2*: These products consists of geo-located geophysical products derived from Level-1. Level-2 Ocean (OCN) products for wind, wave, and currents applications may contain the following geophysical components [47].

For the purpose of this work, we will process the level-0 XML and TIFF products to generate the level-1 SLC and GRD products.

4.3 Experimental Environment

The generation of interferograms and the computation of large time series are computationally expensive tasks and a challenge for current computer technologies. The methodol-

ogy presented in this work takes advantage of many decades of numerical computing and numerical mathematics used under the hood. Furthermore, the satellite data requires considerable storage, usually on the order of terabytes. This characteristic makes it impossible to process meaningful results on a regular laptop or desktop computer.

This project uses a tool constructed on the Generic Mapping Tools (GMT) and GMT-SAR. These tools are open-source and freely available online. Since the generation of interferograms and time series are computationally expensive, these calculations were executed in a High-Performance Computing system.

We used High-Performance Computing (HPC) infrastructure provided by the Ecuadorian Corporation for the Development of Research and Academia (CEDIA) to process the interferograms and compute the time series. We used the NVIDIA DGX A100 HPC system with 256 CPU cores supporting two threads and one terabyte of RAM. It uses the Ubuntu 20.04.2 LTS operating system with the 5.4.0-74 version of the Linux kernel. The current implementation does not take explicit advantage of the GPU capabilities of the system; although, that is a direction we might explore in the future.

4.4 Interferogram Generation

4.4.1 Processing Flow

Firstly, we used the orbit files to determine how the frames match up when combining several images as one. We combined the 280 images before processing, resulting in 184 images available to perform the interferograms. We also cropped the images between -0.3° and 0.4° latitude to focus on our area of interest near Quito (see Fig. 1.3). This preprocessing has two aims. The first is to reduce the size of each image to a specific area of interest, as each Sentinel-1 image typically covers an area of 400km^2 . The second is to decrease the storage needed for the images since each image is 8GB, as we need to consider the storage capabilities of our computing environment.

In the next step, we need to preprocess the input images and generate their products: the Single Look Complex (SLC), parameter (PRM), and leader (LED) files in the GMTSAR format. The SLC file contains the amplitude and phase of each pixel. The PRM and LED files to have metadata related to the image timing and geometry.

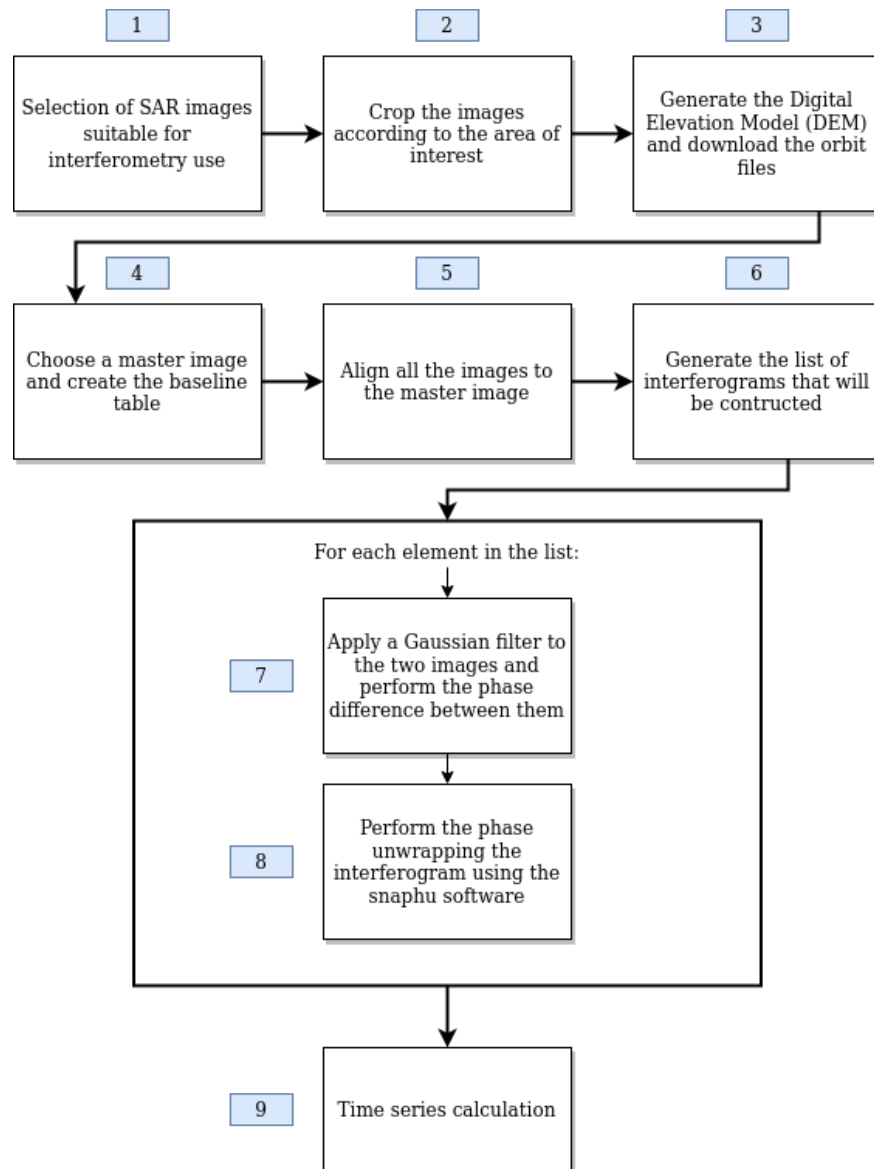


Figure 4.1: Methodology to create interferograms

Further, this step creates the baseline plot. This plot contains information on the perpendicular baseline and the date the satellite took the image. The plot displays each orbit by its time (x-axis) and perpendicular distance from the reference orbit (y-axis).

In the perfect scenario of exact parallel orbits and aligned acquisitions, co-registration would only need to compensate for the differing geometry due to the different view angles [4]. However, that is not the most common case. Instead, we have to choose a 'master' or 'reference' image to which all the others are aligned to achieve the goal of perfectly aligned images.

The reference image needs to be central in the baseline plot between all the images. This baseline plot helps us pair the images and create a list of interferograms that could be constructed (see Fig. 4.2). The selection of interferograms with a short temporal span and a perpendicular baseline is helpful to reduce the noise in the images.

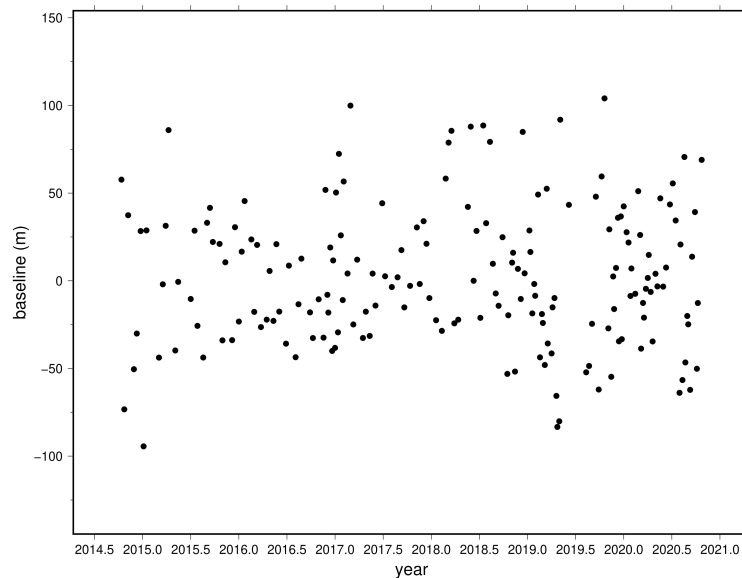


Figure 4.2: Distribution of the used SAR dataset in the temporal (x-axis) and perpendicular baseline (y-axis) plane where the 'master' or 'reference' is located with baseline = 0 which needs to be central in the baseline plot between all the images. This plot helps us as a reference to create different lists of interferograms by connecting pairs of images.

Following this, we need to align the images to the reference image azimuth and slant range (height and width). This alignment is also called co-registration, and it is frequently based on a maximization of the cross-correlation [21].

We pair the images to create as many interferograms as we want. We used a default selection that produced all possible interferograms with fewer than 24 days temporal span.

After that, we calculate the phase difference for each pair of images using the *phasediff* software utility. Then, we reduced the noise produced by the atmospheric effects using a Gaussian filter applied to all the interferograms.

Once we have generated and filtered all the interferograms, we use the SRTM DEM to apply a topographic correction, which accounts for the parallax effect between two images taken with a nonzero perpendicular baseline. Following this correction, we need to do

phase unwrapping. This step was done with the help of the *snaphu* [30] software.

From the computational perspective, the generation of an interferogram requires the following resources: one processor, 8GB of RAM available, and 5 GB of storage available. The execution time of this process takes between 40 to 60 minutes. Each interferogram is processed independently. Thus, we exploit the capabilities of an HPC system by running each interferogram in a different processor while taking care of the RAM usage and storage usage.

We need 8GB of RAM since the required memory is on the order of 100 MB per 1,000,000 pixels in the input interferogram [48]. The size of the images that we are working on is 10,548 x 8,164 pixels.

Finally, we performed geocoding, which involves a transformation from the radar geometry to the coordinates of a selected geodetic reference system[21]. The geocoding process still needs the support of an external reference DEM to obtain more accurate geocoding precision [49].

Fig. 4.1 shows the overall methodology used for the generation of the interferograms.

4.5 Time Series Calculation

Following the computation of the interferograms, we calculate a time series for several different periods using the Small Baseline Subset (SBAS) method.

4.5.1 SBAS approach

For the processing of time series, we used the method described in [32] and the *sbas* software utility of GMTSAR. It consists of the following steps:

- Discriminate the 427 unwrapped interferograms by doing quality control on the interferograms. We discarded 105 of those due to high visible unwrapping errors, atmospheric effects, or missing data. In particular, we omitted the ones collected between 2014 to 2016, when data acquisition was more sparse and with larger baselines. The total number of interferograms that will be used is 322.
- We generated three interferogram lists. The first list contains the 48 interferograms

generated during the year 2017 using 28 SAR images; the second list contains the 56 interferograms generated during the year 2018 using 30 SAR images, and; the third list contains the 218 interferograms generated during the years 2019-2020 using 77 images. See Table 4.1.

- Create the connection graph with the interferograms used for each list of interferograms. See Figure 4.3.
- Run SBAS processing for each list.
- Geo-code the results. We did the conversion of phase units to displacement units and georeferenced the final products.

Table 4.1: Number of interferograms used to generate the time series with the SBAS algorithm grouped by year.

Year(s)	Number of SAR images	Number of Interferograms
2017	28	48
2018	30	56
2019-2020	77	218

We did it on three separate lists because the software requires allocating memory to load all the interferograms. We saw the memory allocation as a disadvantage since the available RAM will be used during all the processing time that could take hours or even days.

4.5.2 ISBAS approach

For the processing of this approach, we used the code available in [50]. We followed the following workflow:

- Discriminate the 184 images by data control. We identified images with missing data using the interferograms that contain missing data. We found 36 images that needed to be discarded; most of them were the ones taken in 2014 and 2015. The time range for this approach is between September 2015 to October 2020, and we will be using 147 images.

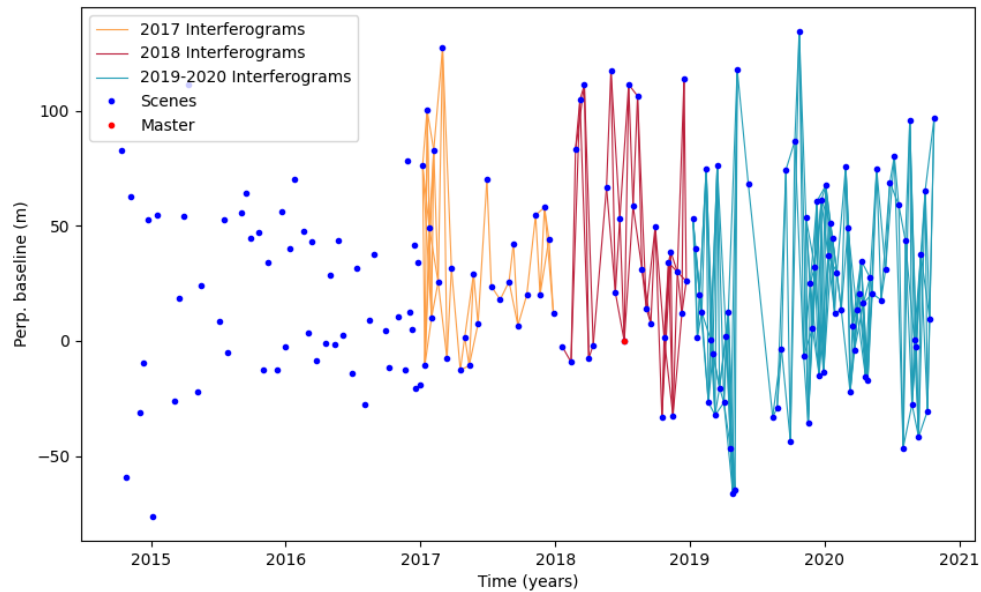


Figure 4.3: Interferograms used to generate the time series using SBAS. Yellow: interferograms generated in 2017. Red: interferograms generated in 2018. Blue: interferograms generated in 2019-2020, the data from 2015 and 2016 were discarded due to the data acquisition was more sparse and with larger baseline.

- Create new interferograms. We need to create new interferograms to make new connections between the images.
- Geocode the interferograms and make sure all of them have the same exterior bounds by padding them with NaN values.
- Create the interferogram lists. We will use three lists with different numbers of interferograms by using the interferograms generated with a 24, 18, and 12 days time span. The first one uses 372 interferograms, the second one uses 269, and the last one uses 169 (See Fig. 4.4).
- Run the experiments.

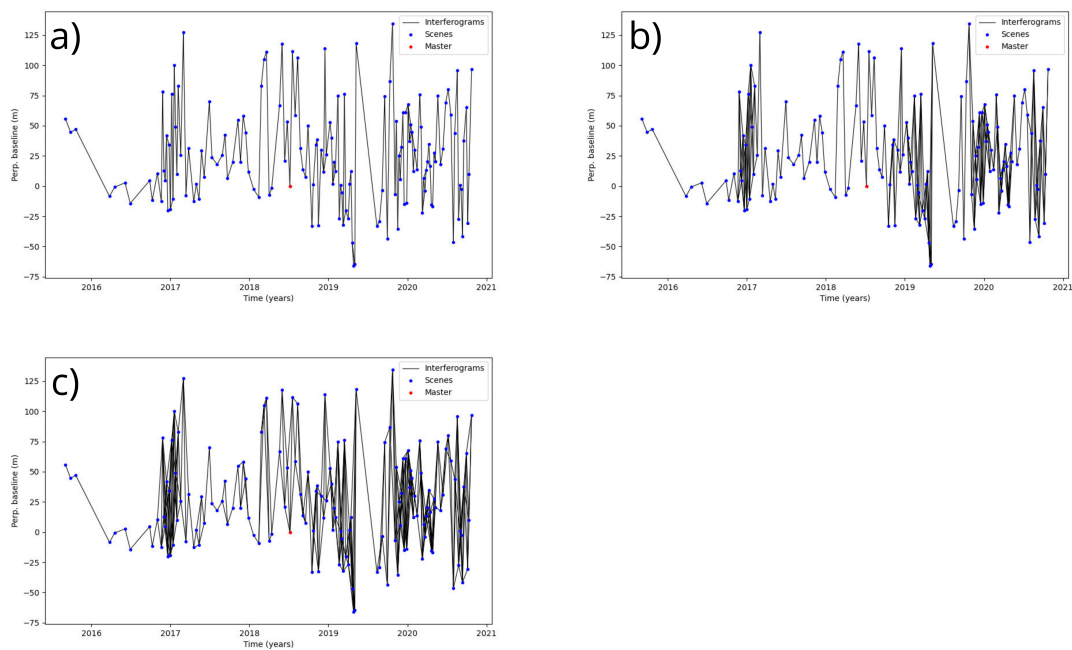


Figure 4.4: Interferograms used to generate the time series using ISBAS. a) 169 generated with a maximum time span of 12 days, b) 269 generated with a maximum time span of 18 days, and c) 372 generated with a maximum time span of 24 days.

Chapter 5

Results

5.1 SBAS results

These results have already been published in [51] and [52]. In this section, we will summarize these results.

Fig. 5.1 shows the obtained time series resulting from InSAR processing of Sentinel 1 images from an ascending orbit order with the SBAS method. Experimental results show good coherence in urban areas and a few large rivers with exposed banks and bars. The lack of coherence in other areas is primarily due to the C-band wavelength, used by the Sentinel satellite, being dispersed by vegetation in other areas.

The mean line-of-sight (LOS) velocities ranges (maximum and minimum), the mean value and the standard deviation are shown in table 5.1. These are relative velocities, and thus the difference between the maximum and minimum values is more important than the absolute velocity. The extreme values in these results could be caused by the two error sources related to the estimation of the ionosphere and troposphere delays.

Table 5.1: Maximum and Minimum values and its locations, Mean and Standard Deviation values calculated of the Mean LOS velocity from SBAS on each subset of interferograms.

Year	Minimum		Maximum		Mean	Standard Deviation
	Mean LOS velocity (mm/yr)	Location (lon/lat)	Mean LOS velocity (mm/yr)	Location (lon/lat)		
2017	-243.80	-78.42°/-0.11°	-88.42	-78.47°/-0.08°	-162.96	10.85
2018	-352.69	-78.52°/-0.33°	-150.12	-78.47°/-0.35°	-259.58	17.58
2019-2020	-270.52	-77.97°/0.04°	-162.10	-77.97°/0.05°	-213.00	8.33

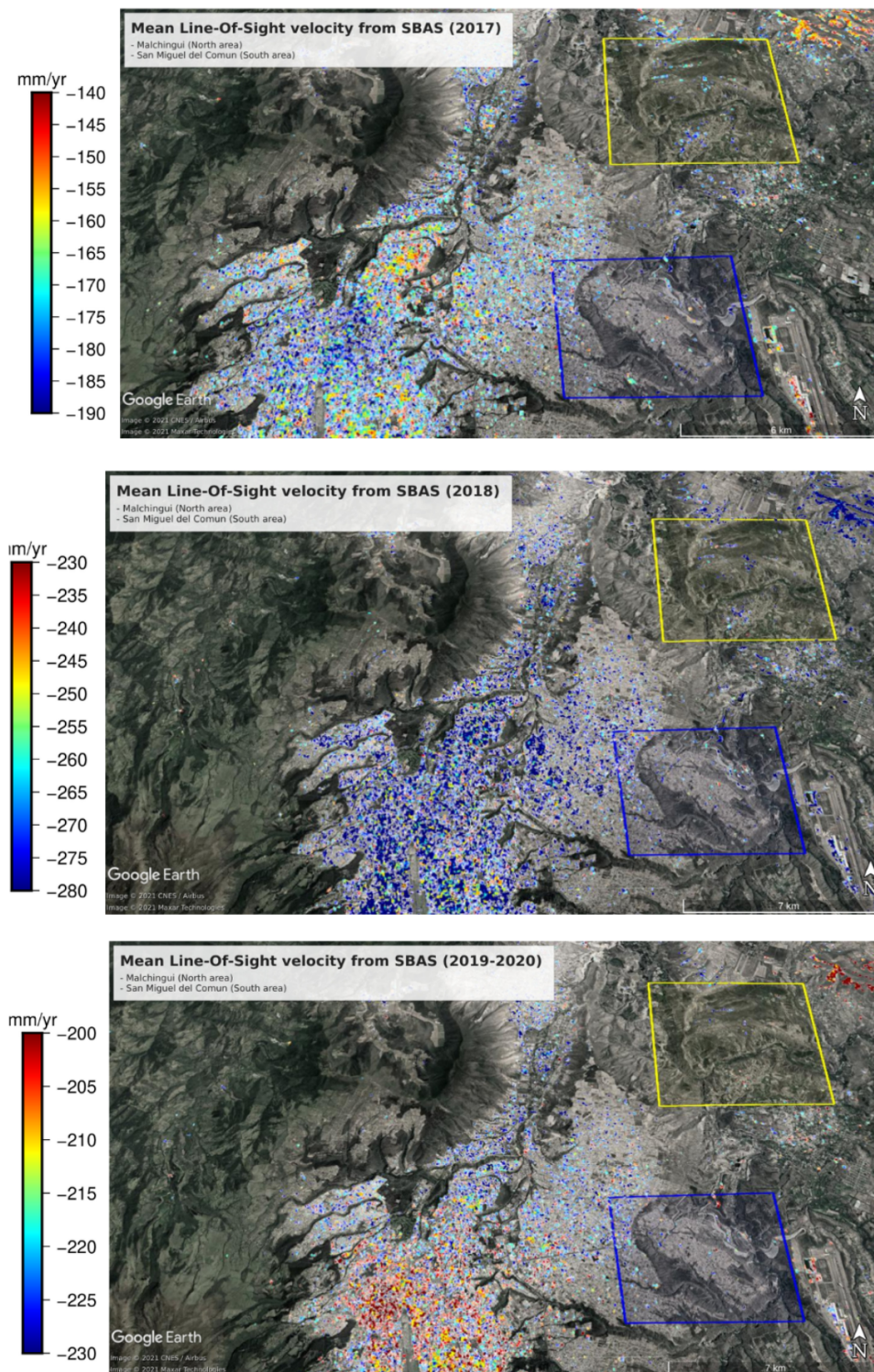


Figure 5.1: Mean Line-of-sight velocities for three time periods, 2017 (top), 2018 (middle), and 2019-2020 (bottom) using SBAS. Two areas of possible active landslides near the Quito Metropolitan Area are shown (Malchingui, yellow box; San Miguel del Comun, blue box). All rates calculated are relative and the zero value is arbitrary.

5.2 ISBAS results

To take advantage of the ISBAS method we performed experiments with the lists of interferograms specified in section 4.5.2, we tested it by generating the time series with different numbers of good interferograms to obtain the maximum number of calculated pixels. Table 5.2 shows the results obtained. It shows that the better results were obtained using 372 interferograms with 320 coherent interferograms as maximum. The mean LOS displacement obtained for the whole region is shown in Figure 5.2. These results showed good coherence in Quito, Otavalo, part of Ibarra, and dry zones. We specify a way to access the time series for any of the pixels calculated in Appendix A.

Table 5.2: Experiments realized to test the ISBAS method.

Number of interferograms	Good Interferograms	Pixels Calculated
160	155	254641
	158	162660
269	260	268846
	263	229245
372	320	502686
	330	451375
	345	355602
	360	254577
	370	125463

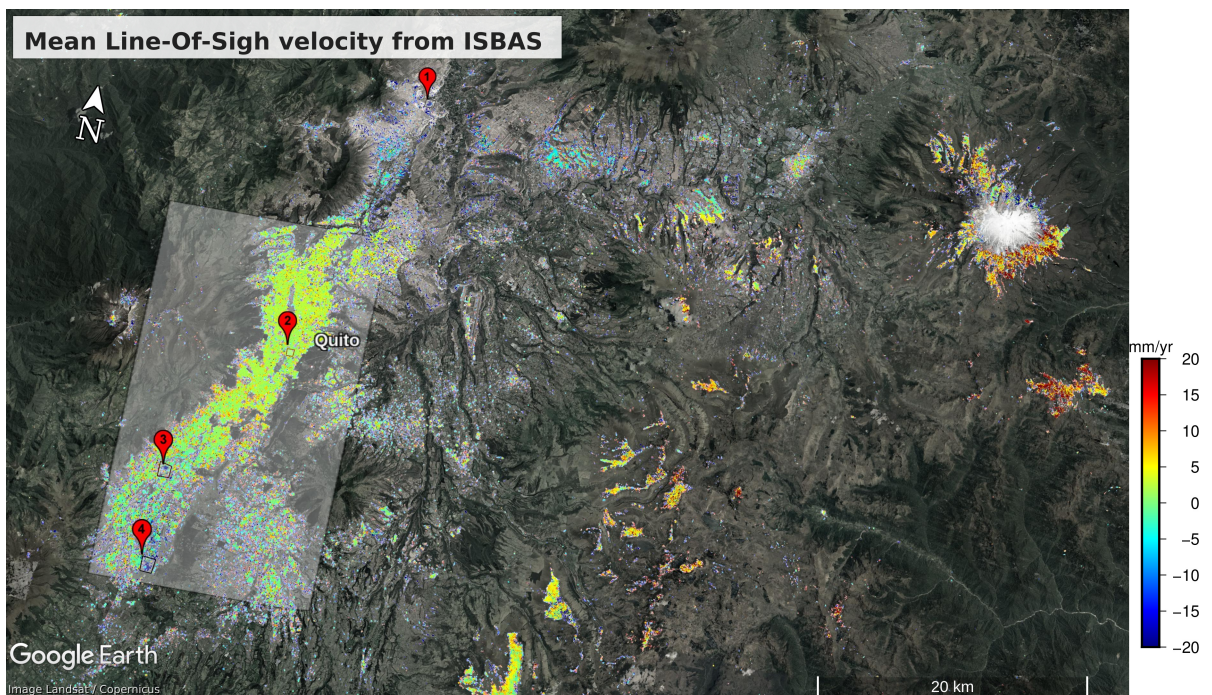


Figure 5.2: Mean Line-of-sight velocities map for the years 2015 to 2020 generated using ISBAS. Red markers are the areas of interest that we discussed in Chapter 6. 1=San Antonio de Quito, 2=Iñaquito parish, 3=Solanda neighborhood, and 4= Pucará neighborhood. The white shaded area was used to create figure 6.5

Chapter 6

Discussion

6.1 Technical Constrains

During the elaboration of this project, we faced software and hardware constraints and problems with the data. The constraint related to the software was the missing dependencies for the installation of GMT and GMTSAR. This problem was solved by compiling all the libraries and software on the home directory. Meanwhile, the hardware limitations are specific to the storage and RAM. We will describe the storage, RAM and, data constraints as follows:

6.1.1 Storage

We need to start by considering that the HPC endowment that we used had 5TB of storage. If we start by downloading a set of Sentinel-1 SLC data and then generate a whole set of interferograms, the process takes a large amount of disk space. In the case of 280 images and 420 interferograms, we need 1.1TB for the downloaded Sentinel 1 products, 125GB for the coregistered SLC data, 5TB for the interferograms (12GB for each, including geo-coded and non-geo-coded data, the filtered and non filtered interferograms, the correlation files, the filter masks, the *kml* files, and others). A total of around 6.5TB of storage for all the files. To complete the goal of generating the 420 interferograms without having a disk space problem, we applied a batch processing of 40 interferograms at a time, deleting the unnecessary files each time we completed a batch. In March 2021, the CEDIA administrators provided 12TB extra for storage. The update helped us to complete all the

products of the processing (all geocoded data).

6.1.2 RAM and processing time

We faced the RAM issue in the generation of the interferograms and while we executed the *sbas* software (included in the GMTSAR tools) for computing the time series. Additionally, we faced the processing time problem in the execution of the *sbas* method.

As we mentioned in section 4.4 the interferograms generation is a costly task, especially the unwrapping step. Due to this, we cannot execute more than 100 interferograms in parallel because this would involve the usage of almost all the available RAM. Another issue was generating the time series since the software will need to allocate memory for the unwrapped non-filtered interferograms, the correlation files, and the estimation of topographic and atmospheric errors for each pixel. This processing will request around 546GB RAM (1.3GB per interferogram) during all the processing time.

The problem related to processing time comes from the main idea of the SBAS method. As suggested in [32] and described in section 2.3, we need to calculate $10,548 \times 8,164$ unique matrix inversions since each matrix contains estimations of the atmospheric and topographic effects. The execution time will increase when we add more interferograms. In the case of our experiments described in section 4.5.1, the execution time was the following for each approach: 48 interferograms 155 minutes, 56 interferograms 212 minutes, and 218 interferograms 3540 minutes. Another solution for this problem was the usage of the code available in [50] which uses the filtered and geo-coded interferograms and reduces the RAM usage and processing time.

We tried to perform SBAS with all the available interferograms, but, in addition to the processing time issue (almost two weeks), we faced the problem of having some interferograms with missing data resulting in time series with few data computed.

6.1.3 Data

The download of the SAR images and elaboration of the interferograms were unsupervised tasks. This methodology leads to having two errors. The first one is related to having missing and poor data on the images taken by the satellite. These problems are visible

when the computations of the time series are complete, so we need to deal with them in different forms.

The missing data in the images led to the creation of time series of regions with high coherence that have no data computed. The pixel with a NaN value will lead to the resulting displacement on that pixel to be NaN (principally in the SBAS method). To deal with this problem, we searched for the images with this problem and dropped them out of the data set as it was mentioned in section 4.5.2 and applied the ISBAS method to create time series and solve the aforementioned problems.

The poor data quality in an image causes problems like unwrapping errors that create unusual jumps in areas where there is not any evidence of land movement like the one shown in the figure 6.1. To avoid this kind of problem, we have two possible solutions: create more interferograms with higher periods to cover that two dates and try to decrease the error or by checking each interferogram individually.

6.2 Malchingui and San Miguel del Comun

The results provided by SBAS (see fig.5.1) show that locations of the maximum and minimum velocities are not near to the two areas that are at risk of land slides. The ISBAS results show that we cannot detect significant mean LOS velocities during the analyzed time period. We could not obtain any notable pixel calculated (mainly related to the vegetation difference across the areas) to detect any possible active landslides in these areas. The implication for this is that these areas are not undergoing creep during this period; however, the site conditions favor landslide development. Earthquakes are a common trigger for catastrophic landslides, and we hope to improve our understanding of the risk for these communities with our continued work.

6.3 San Antonio de Quito

Figure 6.1 shows the deformation in the location of San Antonio de Quito near the Rosita quarry. In this area and all the northern places for which we have coherent results (e.g., Ibarra), we identified an error in the generation of the time series. An unusual jump in the displacement that occurred on the dates June 4 and June 28 of 2016 was caused

by this problem. The origin of the problem is the presence of a unique interferogram created between these two dates. This interferogram has several errors related to the data taken by the satellite, with an error during the unwrapping phase due to the decorrelation phenomena or with the high period between the two images. The interferogram involved is available in Appendix B. It is important to remove this bad interferogram to prevent misinterpretation of the deformation as some sort of rapid subsidence. If we ignore or remove this problem data point, we can observe a tendency of a slow continuous landslide from June 2016 that continues increasing slowly up to 2020 and will probably continue due to the mining activity in the area.

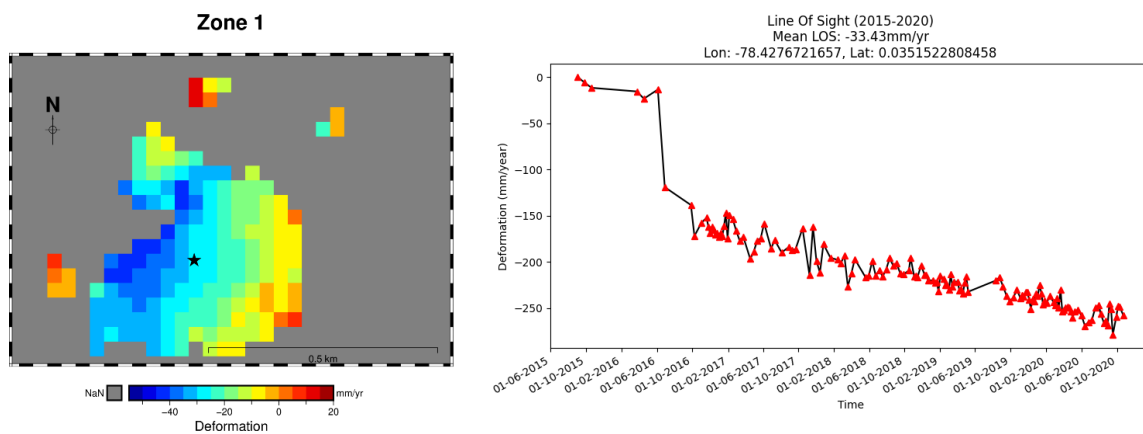


Figure 6.1: Left: Mean Line-of-sight velocities in the area near the Rosita quarry in San Antonio of Pichincha delimited by the polygon $-78.4312/-78.4211/0.0333/0.0394$ (min longitude/max longitude/min latitude/max latitude). Right: Time series of the accumulated displacement in the period between 2015 to 2020 in the location $-78.4276/0.0351$ (lon/lat) indicated by the black star in the left figure. The time series shows one large jump on (date) that is related to an unwrapping error in a single interferogram, rather than a real ground displacement.

6.4 Iñaquito parish of Quito

Figure 6.2 shows a deformation map over the area of Iñaquito in the north of Quito. We can see deformation over this area has an uplift rate of around 0.7mm/yr that predominates in all the nearby areas. In addition, this area does not show any signal of changes in the deformation rate through time.

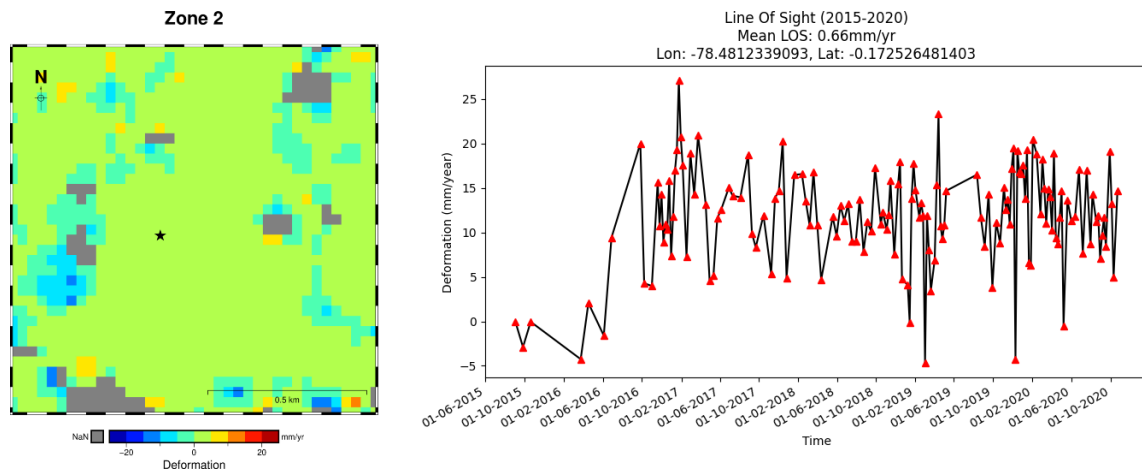


Figure 6.2: Left: Mean Line-of-sight velocities in the Ñaquito parish of Quito near to the Carolina Park delimited by the polygon $-78.4854/-78.4751/-0.1773/-0.1673$ (min longitude/max longitude/min latitude/max latitude). Right: Time series of the accumulated displacement in the period between 2015 to 2020 in the location $-78.4812/-0.1725$ (lon/lat) remarked in the black star in the left figure.

6.5 Solanda neighborhood

Solanda is one of the most populated neighborhoods in Quito. In 2017 started the construction of the Quito subway and a station in the area [53]. The construction company forced a massive groundwater extraction to build this station. That could be the reason for the results obtained in figure 6.3; these results show subsidence caused by the groundwater extraction beginning in 2017 until 2019. This subsidence caused a sinking of about 12cm and several structural problems in the houses of the zone. There are cases of abandoned buildings due to these structural problems [54].

6.6 Pucará neighborhood

This sector is in the extreme south of Quito. We see a constant subsidence signal probably caused by the extraction of groundwater for use in the city. We could not find any registers to corroborate this assumption. Additionally, there are no documented registers of structural problems in the area. The subsidence signal is over 23mm/yr along the LOS direction in the area (see figure 6.4).

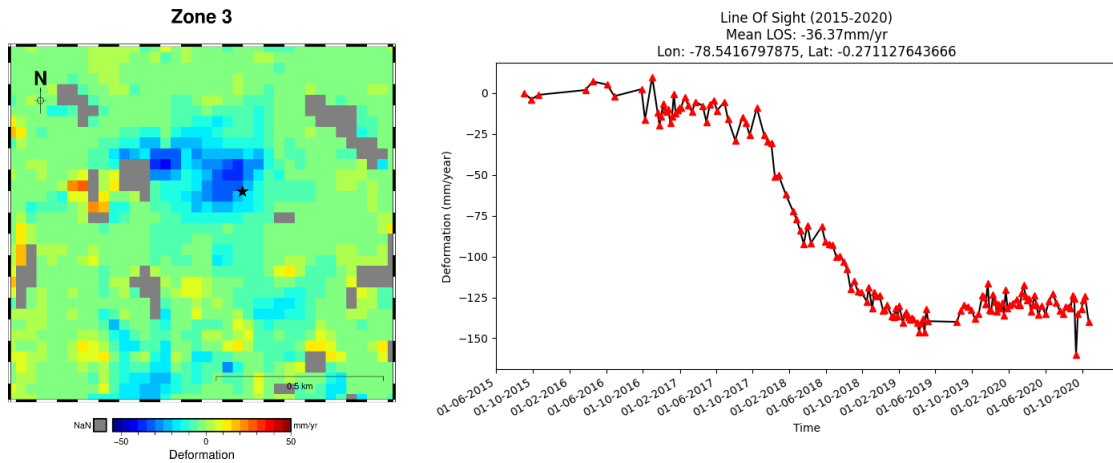


Figure 6.3: Left: Mean Line-of-sight velocities in the south of Quito at the Solanda neighborhood delimited by the polygon $-78.5479/-78.5376/-0.2765/-0.2673$ (min longitude/max longitude/min latitude/max latitude). Right: Time series of the accumulated displacement in the period between 2015 to 2020 in the location $-78.5416/-0.2711$ (lon/lat) indicated by the black star in the left figure.

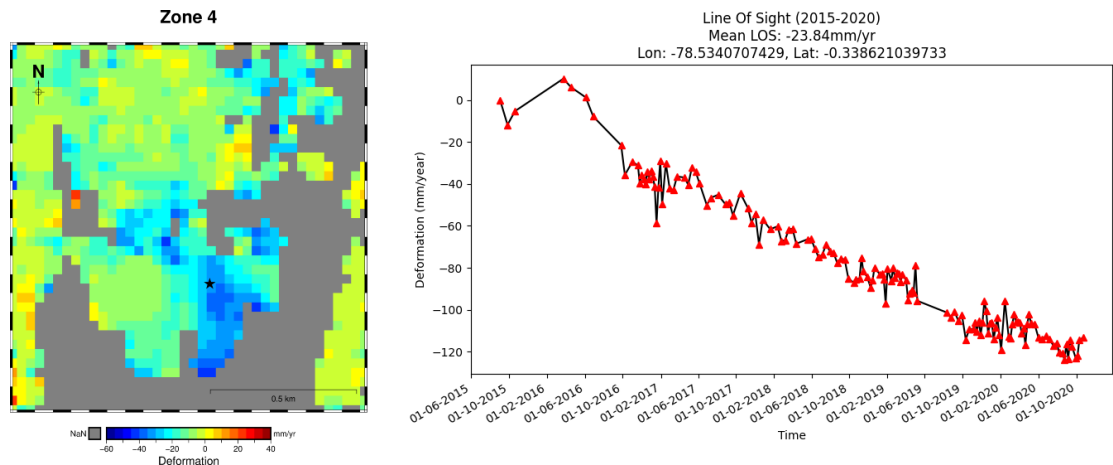


Figure 6.4: Left: Mean Line-of-sight velocities in the south of Quito at the Pucará neighborhood delimited by the polygon $-78.5401/-78.5293/-0.3423/-0.3315$ (min longitude/max longitude/min latitude/max latitude). Right: Time series of the accumulated displacement in the period between 2015 to 2020 in the location $-78.53407/-0.3386$ (lon/lat) indicated by the black star in the left figure.

6.7 Deformation over Quito

We plotted all the points calculated at each latitude between -0.35° to -0.07° covering the urban area of Quito (white shaded area in figure 5.2). We identified a trend on these computed pixels where the density of pixels calculated in south areas shows a subsidence

signal that accommodates up to 2.5mm/yr and in the northern zones, uplift with a rate of 2.5 mm/yr (see figure 6.5). This trend could be related to tectonic deformation from movement on the reverse fault that runs beneath Quito and accommodates 3-5mm/yr of horizontal shortening [19].

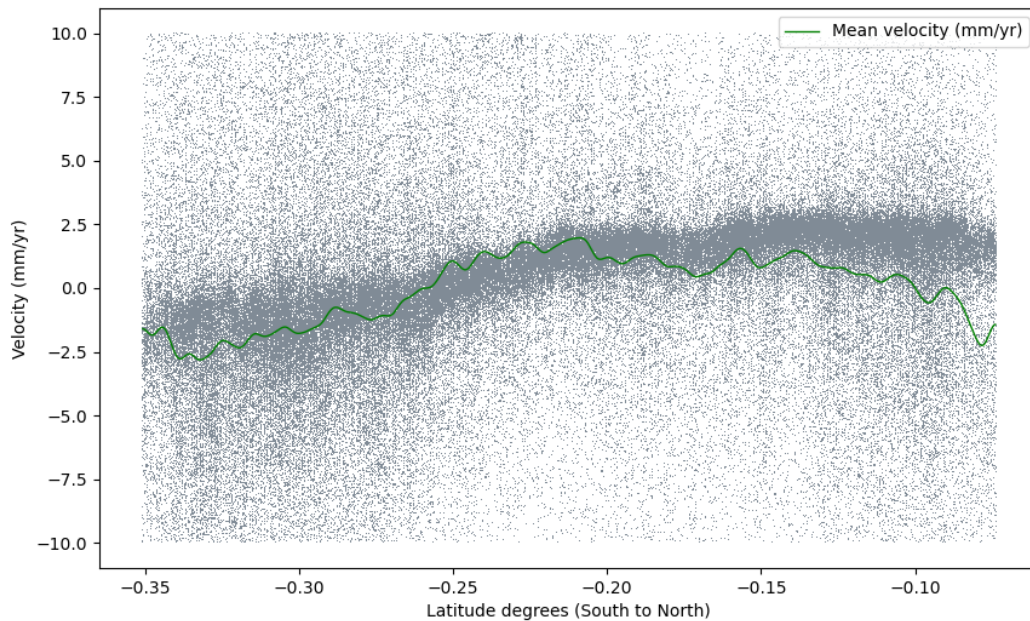


Figure 6.5: Distribution of the mean LOS velocities as a function of latitude for a bin approximately 30 km wide, centered on Quito. The green line represents a smoothed mean velocity of the latitude points.

Chapter 7

Conclusions

7.1 Conclusions

InSAR is a widespread technique used for diverse purposes principally to study certain geological events. We applied this technique over Quito since it is in a zone with multiples sources of seismicity, mining, groundwater, and others. In this work, we described the methodology to create a large set of interferograms and time series. Specifically, we applied the combination of the generation interferograms by the InSAR methodology and the creation of time series using the SBAS and ISBAS methods, which showed a powerful tool to detect a surface deformation or a lack thereof in specific areas.

We were able to compute over 420 interferograms by using the available data of Sentinel 1 over the area of Quito. We then created time series using SBAS and ISBAS. The procedure of creating a large set of interferograms is a costly task and not sensible to the detection of possible errors during the execution and in post-processing stages such as the creation of time series. Other problems that appeared in this project were the storage capacity of the HPC since it restricted the availability of the products of the generated interferograms and the processing time (for the SBAS method). The CEDIA HPC administration addressed the storage problem indirectly by adding more storage capacity. Meanwhile, we solved the processing time problem by usage of the ISBAS method.

The results obtained show high coherence in urban and dry zones, while vegetated areas like parks, and rural places with dense vegetation and high agricultural use showed bad coherence. These results are due to the properties of the C-band frequency of Sentinel-1.

We detected several deformation sources in different areas and estimated the mean rate of deformation in Quito. We determined that two target areas (Malchingui and San Miguel del Comun) for potential landslide hazards do not show ground deformation during the studied period using SBAS and ISBAS. This result does not signify any active creep but does not preclude catastrophic landslides in the future. Additionally, we used the ISBAS results to find interest areas. We found two areas (Pucará and San Antonio de Pichincha) for potential landslide hazards caused by groundwater extraction and mining activities. There is a specific zone (Solanda) where we found rapid deformation in a small window of time that already has caused problems for the residents of the area. Finally, ISBAS results show an approximate LOS rate of deformation of $\pm 2.5\text{mm/yr}$ due to the Quito Fault System, consistent with the estimates from [19].

In general, the creation of interferograms, the generation of the time series, and the analysis of some areas with deformation accomplished the general and specific objectives outlined in chapter 1.

7.2 Future Work

The availability of Sentinel 1 images is each 11 days. For this reason, we expect to improve these results by adding more images to the time series by optimizing the processing time using low level frameworks such as Open Computing Language (OpenCL) and Compute Unified Device Architecture (CUDA).

Furthermore, there is the possibility of applying unsupervised and supervised machine learning algorithms for different purposes such as terrain and surface displacement classification. Another challenge is the identification of bad interferograms or unwrapping errors that introduce false jumps into the time series.

In addition to expanding the Sentinel results, we have 60 scenes from the ALOS-2 satellite provided by JAXA through a data grant that we will process for the same areas. The longer wavelength of the ALOS-2 satellite signal (L-band) allows it to penetrate clouds, fog, rain, storms, and vegetation. These characteristics will permit us to create interferograms over a much wider area where we have a loss of coherence in the Sentinel data, such as in the zone of the Chingual fault segment, which is thought to be active at a rate of

approximately 8 mm/yr and represents a source of hazard for northern Ecuador.

Bibliography

- [1] P. Euillades, L. Euillades, A. Pepe, P. Mastro, F. Falabella, P. Imperatore, Y. Tang, and P. Rosell, “Recent advancements in multi-temporal methods applied to new generation SAR systems and applications in south america,” *Journal of South American Earth Sciences*, vol. 111, p. 103410, Nov. 2021. [Online]. Available: <https://doi.org/10.1016/j.jsames.2021.103410>
- [2] C. Beauval, H. Yepes, W. H. Bakun, J. Egred, and A. Alvarado, “Locations and magnitudes of historical earthquakes in the sierra of ecuador (1587-1996),” *Geophysical Journal International*, Apr. 2010, doi: 10.1111/j.1365-246x.2010.04569.x.
- [3] C. Beauval, J. Marinière, H. Yepes, L. Audin, J.-M. Nocquet, A. Alvarado, S. Baize, J. Aguilar, J.-C. Singaicho, and H. Jomard, “A new seismic hazard model for ecuador,” vol. 108, no. 3A, pp. 1443–1464, Apr. 2018. [Online]. Available: <https://doi.org/10.1785/0120170259>
- [4] A. Ferretti, A. Monti-Guarnieri, C. Prati, and R. F., *InSAR Principles: Guidelines for SAR Interferometry Processing and Interpretation*, 3rd ed. The Netherlands: ESA Publications Division, 2007.
- [5] F. Casu, M. Manzo, and R. Lanari, “Performance analysis of the sbas algorithm for surface deformation retrieval,” *European Space Agency, (Special Publication) ESA SP*, vol. 610, p. 12, 01 2006.
- [6] A. Pepe and F. Calò, “A review of interferometric synthetic aperture radar (insar) multi-track approaches for the retrieval of earth’s surface displacements,” *Applied Sciences*, vol. 7, no. 12, 2017. [Online]. Available: <https://www.mdpi.com/2076-3417/7/12/1264>

- [7] A. M. Ruiz-Armenteros, J. manuel Delgado, B. J. Ballesteros-Navarro, M. Lazecky, M. Bakon, and J. J. Sousa, “Deformation monitoring of the northern sector of the valencia basin (e spain) using ps-insar (1993–2010),” in *IGARSS 2018 - 2018 IEEE International Geoscience and Remote Sensing Symposium*, Jul. 2018. [Online]. Available: doi:10.1109/igarss.2018.8519126
- [8] J. Biggs, P. Mothes, M. Ruiz, F. Amelung, T. H. Dixon, S. Baker, and S.-H. Hong, “Stratovolcano growth by co-eruptive intrusion: The 2008 eruption of tungurahua ecuador,” *Geophysical Research Letters*, vol. 37, no. 21, pp. n/a–n/a, Nov. 2010. [Online]. Available: <https://doi.org/10.1029/2010gl044942>
- [9] R. Rosana, F. T. José, R. V. Gema, A. Vicente, A. Alfredo, C. Daniel, L. Francisco, M. Victoriano, and M. Antonio, “Synthetic aperture radar interferometry (insar): Application to ground deformation studies for volcano and seismic monitoring,” *Física de la Tierra*, 2002. [Online]. Available: <http://hdl.handle.net/10261/6597>
- [10] J. Champenois, V. Pinel, S. Baize, L. Audin, H. Jomard, A. Hooper, A. Alvarado, and H. Yepes, “Large-scale inflation of tungurahua volcano (ecuador) revealed by persistent scatterers SAR interferometry,” *Geophysical Research Letters*, vol. 41, no. 16, pp. 5821–5828, Aug. 2014. [Online]. Available: <https://doi.org/10.1002/2014gl060956>
- [11] A. M. M. Rivera, F. Amelung, and P. Mothes, “Volcano deformation survey over the northern and central andes with ALOS InSAR time series,” *Geochemistry, Geophysics, Geosystems*, vol. 17, no. 7, pp. 2869–2883, Jul. 2016. [Online]. Available: <https://doi.org/10.1002/2016gc006393>
- [12] T. J. Fournier, M. E. Pritchard, and S. N. Riddick, “Duration, magnitude, and frequency of subaerial volcano deformation events: New results from latin america using InSAR and a global synthesis,” *Geochemistry, Geophysics, Geosystems*, vol. 11, no. 1, pp. n/a–n/a, Jan. 2010. [Online]. Available: <https://doi.org/10.1029/2009gc002558>
- [13] A. M. M. Rivera, F. Amelung, P. Mothes, S.-H. Hong, J.-M. Nocquet, and P. Jarrin, “Ground deformation before the 2015 eruptions of cotopaxi volcano detected by

- InSAR,” *Geophysical Research Letters*, vol. 44, no. 13, pp. 6607–6615, Jul. 2017. [Online]. Available: <https://doi.org/10.1002/2017gl073720>
- [14] M. Cando-Jácome, A. Martínez-Graña, K. Chunga, and E. Ortiz-Hernández, “Satellite radar interferometry for assessing coseismic liquefaction in portoviejo city, induced by the mw 7.8 2016 pedernales, ecuador earthquake,” *Environmental Earth Sciences*, vol. 79, no. 19, Sep. 2020. [Online]. Available: <https://doi.org/10.1007/s12665-020-09205-x>
- [15] K. B. Kwong, H. R. DeShon, J. W. Kim, and Z. Lu, “Resolving teleseismic earthquake catalog and InSAR data discrepancies in absolute space to explore rupture complexity along the ecuadorian megathrust fault,” *Journal of Geophysical Research: Solid Earth*, vol. 124, no. 7, pp. 6703–6719, Jul. 2019. [Online]. Available: <https://doi.org/10.1029/2018jb016271>
- [16] J.-M. Nocquet, P. Jarrin, M. Vallée, P. A. Mothes, R. Grandin, F. Rolandone, B. Delouis, H. Yepes, Y. Font, D. Fuentes, M. Régnier, A. Laurendeau, D. Cisneros, S. Hernandez, A. Sladen, J.-C. Singaicho, H. Mora, J. Gomez, L. Montes, and P. Charvis, “Supercycle at the ecuadorian subduction zone revealed after the 2016 pedernales earthquake,” *Nature Geoscience*, vol. 10, no. 2, pp. 145–149, Dec. 2016. [Online]. Available: <https://doi.org/10.1038/ngeo2864>
- [17] J. Champenois, S. Baize, M. Vallee, H. Jomard, A. Alvarado, P. Espin, G. Ekström, and L. Audin, “Evidences of surface rupture associated with a low-magnitude (m w 5.0) shallow earthquake in the ecuadorian andes,” *Journal of Geophysical Research: Solid Earth*, vol. 122, no. 10, pp. 8446–8458, Oct. 2017. [Online]. Available: <https://doi.org/10.1002/2017jb013928>
- [18] S. Baize, L. Audin, T. Winter, A. Alvarado, L. P. Moreno, M. Taipe, P. Reyes, P. Kauffmann, and H. Yepes, “Paleoseismology and tectonic geomorphology of the pallatanga fault (central ecuador), a major structure of the south-american crust,” *Geomorphology*, vol. 237, pp. 14–28, May 2015. [Online]. Available: <https://doi.org/10.1016/j.geomorph.2014.02.030>

- [19] J. Marinier, J.-M. Nocquet, C. Beauval, J. Champenois, L. Audin, A. Alvarado, S. Baize, and A. Socquet, “Geodetic evidence for shallow creep along the quito fault, ecuador,” *Geophysical Journal International*, vol. 220, no. 3, pp. 2039–2055, Dec. 2019. [Online]. Available: <https://doi.org/10.1093/gji/ggz564>
- [20] P. A. Espín-Bedón, L. Audin, M.-P. Doin, E. Pathier, F. Tollard, C. Laurent, A. Alvarado, J. Marinier, P. Ann-Mothes, M. Segovia, S. Vaca, and C. Beauval, “Deformation monitoring from synthetic aperture radar interferometry (insar) sentinel data in quito, ecuador,” in *8th International Symposium on Andean Geodynamics (ISAG)*, Sep. 24-26 2019. [Online]. Available: <https://www.igepn.edu.ec/8isag-abstracts/active-tectonics-deformation/22713-espin-bedon-et-al/file>
- [21] A. Moreira, P. Prats-Iraola, M. Younis, G. Krieger, I. Hajnsek, and K. P. Papathanassiou, “A tutorial on synthetic aperture radar,” *IEEE Geosci. Remote Sens. Mag.*, vol. 1, p. 6–43, Mar. 2013, doi: 10.1109/mgrs.2013.2248301.
- [22] R. Hanssen, *Radar interferometry : data interpretation and error analysis*. S.l: s.n., 2001.
- [23] H. Zebker and J. Villasenor, “Decorrelation in interferometric radar echoes,” *IEEE Transactions on Geoscience and Remote Sensing*, vol. 30, no. 5, pp. 950–959, 1992. [Online]. Available: <https://doi.org/10.1109/36.175330>
- [24] R. Touzi, A. Lopes, J. Bruniquel, and P. Vachon, “Coherence estimation for SAR imagery,” *IEEE Transactions on Geoscience and Remote Sensing*, vol. 37, no. 1, pp. 135–149, 1999. [Online]. Available: <https://doi.org/10.1109/36.739146>
- [25] M. Wei and D. T. Sandwell, “Decorrelation of l-band and c-band interferometry over vegetated areas in california,” *IEEE Transactions on Geoscience and Remote Sensing*, vol. 48, no. 7, pp. 2942–2952, Jul. 2010. [Online]. Available: <https://doi.org/10.1109/tgrs.2010.2043442>
- [26] F. Onn and H. A. Zebker, “Correction for interferometric synthetic aperture radar atmospheric phase artifacts using time series of zenith wet delay observations from

- a GPS network,” *Journal of Geophysical Research*, vol. 111, no. B9, 2006. [Online]. Available: <https://doi.org/10.1029/2005jb004012>
- [27] C. Yu, Z. Li, N. T. Penna, and P. Crippa, “Generic atmospheric correction model for interferometric synthetic aperture radar observations,” *Journal of Geophysical Research: Solid Earth*, vol. 123, no. 10, pp. 9202–9222, Oct. 2018. [Online]. Available: <https://doi.org/10.1029/2017jb015305>
- [28] E. Tymofyeyeva and Y. Fialko, “Mitigation of atmospheric phase delays in InSAR data, with application to the eastern california shear zone,” *Journal of Geophysical Research: Solid Earth*, vol. 120, no. 8, pp. 5952–5963, Aug. 2015. [Online]. Available: <https://doi.org/10.1002/2015jb011886>
- [29] C. Chen and H. Zebker, “Phase unwrapping for large SAR interferograms: statistical segmentation and generalized network models,” *IEEE Transactions on Geoscience and Remote Sensing*, vol. 40, no. 8, pp. 1709–1719, Aug. 2002. [Online]. Available: <https://doi.org/10.1109/tgrs.2002.802453>
- [30] C. W. Chen and H. A. Zebker, “Two-dimensional phase unwrapping with use of statistical models for cost functions in nonlinear optimization,” *Journal of the Optical Society of America A*, vol. 18, no. 2, p. 338, Feb. 2001. [Online]. Available: <https://doi.org/10.1364/josaa.18.000338>
- [31] —, “Network approaches to two-dimensional phase unwrapping: intractability and two new algorithms,” *Journal of the Optical Society of America A*, vol. 17, no. 3, p. 401, Mar. 2000. [Online]. Available: <https://doi.org/10.1364/josaa.17.000401>
- [32] P. Berardino, G. Fornaro, R. Lanari, and E. Sansosti, “A new algorithm for surface deformation monitoring based on small baseline differential sar interferograms,” *IEEE Trans. Geosciences and Remote Sensing*, vol. 40, p. 2375–2383, 2002.
- [33] A. Ferretti, C. Prati, and F. Rocca, “Permanent scatterers in SAR interferometry,” *IEEE Transactions on Geoscience and Remote Sensing*, vol. 39, no. 1, pp. 8–20, 2001. [Online]. Available: <https://doi.org/10.1109/36.898661>

- [34] R. Lanari, F. Casu, M. Manzo, G. Zeni, P. Berardino, M. Manunta, and A. Pepe, “An overview of the small BAseLine subset algorithm: a DInSAR technique for surface deformation analysis,” *Pure and Applied Geophysics*, vol. 164, no. 4, pp. 637–661, Apr. 2007. [Online]. Available: <https://doi.org/10.1007/s00024-007-0192-9>
- [35] A. Sowter, L. Bateson, P. Strange, K. Ambrose, and M. F. Syafiudin, “DInSAR estimation of land motion using intermittent coherence with application to the south derbyshire and leicestershire coalfields,” *Remote Sensing Letters*, vol. 4, no. 10, pp. 979–987, Oct. 2013. [Online]. Available: <https://doi.org/10.1080/2150704x.2013.823673>
- [36] M. Manunta, C. D. Luca, I. Zinno, F. Casu, M. Manzo, M. Bonano, A. Fusco, A. Pepe, G. Onorato, P. Berardino, P. D. Martino, and R. Lanari, “The parallel SBAS approach for sentinel-1 interferometric wide swath deformation time-series generation: Algorithm description and products quality assessment,” *IEEE Transactions on Geoscience and Remote Sensing*, vol. 57, no. 9, pp. 6259–6281, Sep. 2019. [Online]. Available: <https://doi.org/10.1109/tgrs.2019.2904912>
- [37] F. Casu, S. Elefante, P. Imperatore, I. Zinno, M. Manunta, C. D. Luca, and R. Lanari, “SBAS-DInSAR parallel processing for deformation time-series computation,” *IEEE Journal of Selected Topics in Applied Earth Observations and Remote Sensing*, vol. 7, no. 8, pp. 3285–3296, Aug. 2014. [Online]. Available: <https://doi.org/10.1109/jstars.2014.2322671>
- [38] F. Monterroso, I. Zinno, F. Casu, M. Bonano, C. D. Luca, V. D. Novellis, R. Lanari, M. Manunta, M. Manzo, G. Onorato, and E. Valerio, “Unsupervised and automatic generation of DInSAR co-seismic displacement maps by means of sentinel-1 data,” in *IGARSS 2019 - 2019 IEEE International Geoscience and Remote Sensing Symposium*. IEEE, Jul. 2019. [Online]. Available: <https://doi.org/10.1109/igarss.2019.8898772>
- [39] F. Cigna, D. Tapete, J. Danzeglocke, P. Bally, R. Cuccu, T. Papadopoulou, H. Caumont, A. Collet, H. de Boissezon, A. Eddy, and B. Piard, “Supporting recovery after 2016 hurricane matthew in haiti with big SAR data processing in the geohazards exploitation platform (GEP),” in *IGARSS 2020 - 2020 IEEE*

- International Geoscience and Remote Sensing Symposium*. IEEE, Sep. 2020. [Online]. Available: <https://doi.org/10.1109/igarss39084.2020.9323231>
- [40] S. Pepe, L. D’Auria, R. Castaldo, F. Casu, C. D. Luca, V. D. Novellis, E. Sansosti, G. Solaro, and P. Tizzani, “The use of massive deformation datasets for the analysis of spatial and temporal evolution of mauna loa volcano (hawai’i),” *Remote Sensing*, vol. 10, no. 6, p. 968, Jun. 2018. [Online]. Available: <https://doi.org/10.3390/rs10060968>
- [41] G. Hager and G. Wellein, *Introduction to High Performance Computing for Scientists and Engineers*. FL, USA: CRC Press: Boca Raton, 2010.
- [42] A. Pepe and R. Lanari, “On the extension of the minimum cost flow algorithm for phase unwrapping of multitemporal differential SAR interferograms,” *IEEE Transactions on Geoscience and Remote Sensing*, vol. 44, no. 9, pp. 2374–2383, Sep. 2006. [Online]. Available: <https://doi.org/10.1109/tgrs.2006.873207>
- [43] M. Lazecký, K. Spaans, P. J. González, Y. Maghsoudi, Y. Morishita, F. Albino, J. Elliott, N. Greenall, E. Hatton, A. Hooper, D. Juncu, A. McDougall, R. J. Walters, C. S. Watson, J. R. Weiss, and T. J. Wright, “LiCSAR: An automatic InSAR tool for measuring and monitoring tectonic and volcanic activity,” *Remote Sensing*, vol. 12, no. 15, p. 2430, Jul. 2020. [Online]. Available: <https://doi.org/10.3390/rs12152430>
- [44] O. Hogoiu and M. Peters, “Science toolbox exploitation platform,” Jun 2021. [Online]. Available: <http://step.esa.int/main/>
- [45] P. Wessel, W. H. F. Smith, R. Scharroo, J. Luis, and F. Wobbe, “Generic mapping tools: Improved version released,” *Eos, Transactions American Geophysical Union*, vol. 94, no. 45, pp. 409–410, Nov. 2013. [Online]. Available: <https://doi.org/10.1002/2013eo450001>
- [46] D. Sandwell, R. Mellors, X. Tong, M. Wei, and P. Wessel, “Gmtsar: An insar processing system based on generic mapping tools,” May 2011. [Online]. Available: <https://escholarship.org/uc/item/8zq2c02m#author>

- [47] K. Fletcher, *Sentinel-1: ESA's Radar Observatory Mission for GMES Operational Services*, 1st ed. ESA Communications, 2012.
- [48] "SNAPHU: Statistical-Cost, Network-Flow Algorithm for Phase Unwrapping," <https://web.stanford.edu/group/radar/softwareandlinks/sw/snaphu/>, 2020, online; accessed 10-August-2021.
- [49] L. Zhao, E. Chen, Z. Li, W. Zhang, Y. Fan, , and X. Wan, "The synergetic estimation approach of forest above ground biomass based on x-band insar and p-band polsar data," in *IGARSS 2018 - 2018 IEEE International Geoscience and Remote Sensing Symposium*, Jul. 2018. [Online]. Available: doi:10.1109/igarss.2018.8518175
- [50] E. O. Lindsey, "Isbas: Intermittent small baseline subset insar timeseries algorithm," <https://github.com/ericlindsey/isbas>, 2021.
- [51] J. Goyes, A. E. Foster, E. O. Lindsey, R. V. Almeida, and I. Pineda, "Constraining interseismic deformation in northern ecuador using interferometry of sentinel-1 and alos-2 data," in *AGU Fall Meeting 2020*. AGU, 2020.
- [52] J. Goyes, I. Pineda, E. Lindsey, A. Foster, and R. Almeida, "Constraining interseismic deformation of northern ecuador using interferometry from sentinel-1 data," in *2021 Second International Conference on Information Systems and Software Technologies (ICI2ST)*. IEEE, Mar. 2021. [Online]. Available: <https://doi.org/10.1109/ici2st51859.2021.00013>
- [53] V. Silva Cruz. (2021) En solanda, al sur de quito, 43 casas están destruidas y 233 presentan daños; sus propietarios exigen soluciones, pero ni la empresa que construye el metro ni la alcaldía responden. [Online]. Available: <https://bit.ly/3aIVbvJ>
- [54] E. Jácome. (2021) Dueños de casas afectadas en solanda, sur de quito, aún sin respuesta. [Online]. Available: <https://bit.ly/2WWytqH>

Appendices

Appendix A. ISBAS results

The results obtained by the ISBAS method using 320 good interferograms of 372 interferograms are available in <https://github.com/jjjggg092/ISBAS-results>. We will describe how to extract time series from the data obtained:

Description

The script `plot_ts.py` allows to read all the files result of executing the ISBAS method from this repository and create a plot with the time series displacement of a specific location.

Files

- **baseline_table.dat:** file with information about the acquisition dates of the images.
- **rate_mm_yr.grd:** NetCDF 4 file with all the data calculated to obtain the mean displacement between 2015 and 2020.
- **rate_mm_yr.kml:** Google Earth file to visualize the results obtained.
- **rate_mm_yr.png:** Supplement of the *rate_mm_yr.kml* to see the results.

Requirements

Software

- Python 3
- The Generic Mapping Tools (GMT)

Python libraries

- Numpy
- Matplotlib

Usage

```
python3 plot_ts.py (disp_file.txt) (latitude) (longitude)
```

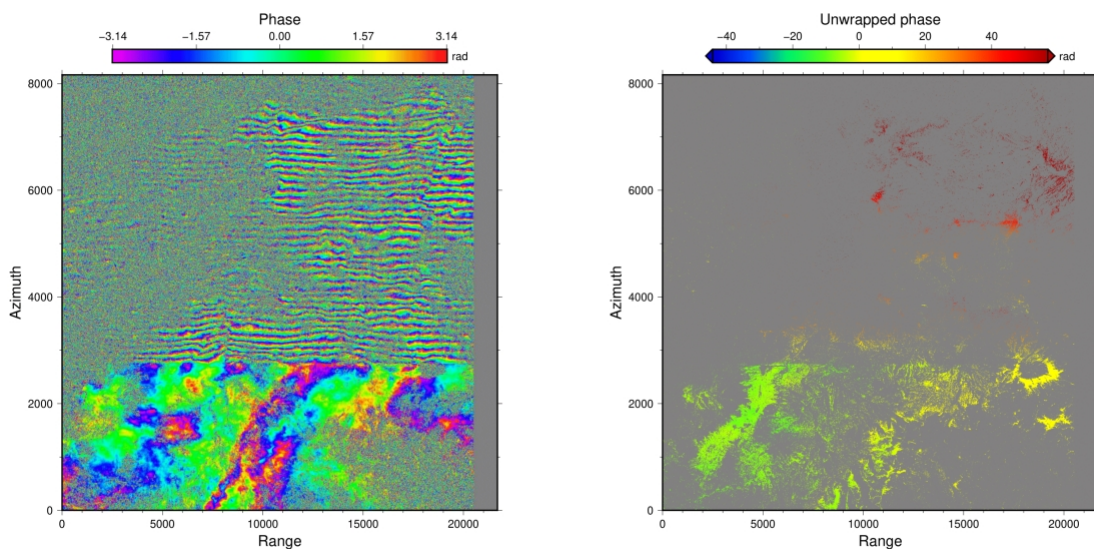
where:

- **disp_file.txt:** A file with all the locations of the grd files with the information about displacements.
- **latitude:** The latitude reference in decimal degrees.
- **longitude:** The longitude reference in decimal degrees.

Example:

```
python3 plot_ts.py files.txt 0.0352876437857 -78.4276493471
```

Appendix B. Interferogram generated with the scenes taken in June 4 and June 28 of 2016



A bad interferogram that caused an anomaly subsidence event in north areas. Left: wrapped interferogram. Right: unwrapped interferogram